The IRM Quarterly
Spring 2022, Vol. 32 No. 1
ISSN: 2152-1972

Inside...

Practical Magnetism VIII: reporting and visualization of magnetic anisotropy data

Dario Bilardello
Institute for Rock Magnetism
dario@umn.edu

Andrea R. Biedermann
University of Bern
andrea.biedermann@geo.unibe.ch

1 Applications of magnetic anisotropy data

Magnetic fabrics are a powerful, rapid and non-destructive tool to characterize mineral alignment and dynamic processes, and as such are widely applied in structural geology and tectonics, volcanology, sedimentology, and pore fabric studies. Rock deformation, sediment transport and compaction, lava and pyroclastic flow directions and emplacement of igneous bodies are some examples of processes that can be studied using magnetic anisotropy. Furthermore, paleomagnetic remanence data may exhibit a dependence on the magnetic fabric and magnetic anisotropy can be used to correct those data. Different minerals, including the characteristic remanence carriers, contribute differently to the observed magnetic fabrics, and understanding their contributions to the anisotropy allows better interpretation of geodynamic processes and paleomagnetic data (e.g., Biedermann & Bilardello, 2021, IRMQ31-3).

Numerous anisotropy parameters and ways to visualize magnetic fabric data exist, and choice of parameters and plots to use is by no-means homogeneous across the different research communities. Choice of parameters is often adapted to the specific application: for example, certain parameters for lineation (L) and foliation (F), more below, are often used for structural geology because they relate to the equivalent parameters as derived from other strain markers and are often plotted against each other as conventionally done for strain ratios (e.g., see Tarling & Hrouda (1993) for a more extensive discussion). Likewise, in "applied" magnetic fabric studies, the anisotropy degree is commonly described by the parameters P or P_J (also referred to as P'); however, studies that focus on single crystals' magnetocrystalline anisotropy more commonly use the Δk or k' parameters.

Describing non-ellipsoidal particles or quantities is even more complex, and requires additional parameters, such as roundness, angularity, sphericity, or irregularity (e.g., Blott & Pye, 2007). Similarly, complicated anisotropies arising from higher-order tensors need additional descriptors (e.g., Biedermann et al., 2020; Flanders &

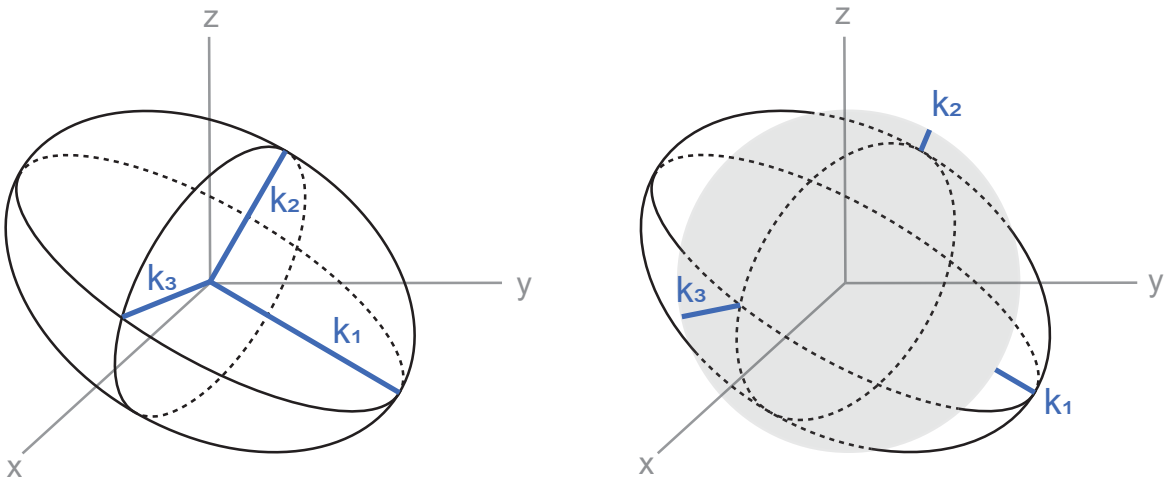

Figure 1. Schematic representation of full vs deviatoric tensors. In full tensors, the eigenvalues correspond to the semi axes of the anisotropy ellipsoid, whereas in the deviatoric tensors, the eigenvalues are defined as the difference between the semi axes of the ellipsoid and the "isotropic radii" approximated by the mean susceptibility k_m.

cont'd. on pg. 10...

Visiting Fellow Reports

Magnetofossils, with a side of siderite, in PETM sediments from Wilson Lake, New Jersey

Courtney Wagner
Smithsonian Institution, National Museum of Natural History, Washington D.C.

Department of Geology & Geophysics, University of Utah, Salt Lake City, U.T.

wagnerc@si.edu

The Paleocene-Eocene Thermal Maximum (PETM, ~56 Ma ago) is the largest carbon cycle perturbation of the Cenozoic (Westerhold et al., 2020). Although the rate of warming during the PETM pales in comparison to the Anthropocene, it is one of the best natural analogs for understanding and predicting outcomes associated with modern climate change (McInerney & Wing, 2011; Zeebe et al., 2016). It is globally identified by a negative carbon isotope excursion (CIE) (Kennett & Stott, 1991; Thomas & Shackleton, 1996) and is best described by six stratigraphic intervals that reflect the structure of the CIE: the pre-CIE, CIE onset, CIE core, CIE recovery phase I, CIE recovery phase II, and post-CIE intervals (Westerhold et al., 2018).

The CIE is recorded at high temporal resolution within the Marlboro Clay that was deposited along the Paleogene New Jersey, Maryland, and Delaware coast (Bralower et al., 2018; John et al., 2008; Kent et al., 2003; Self-Trail et al., 2012, 2017; Stassen et al., 2012; Zachos et al., 2006). The magnitude of the CIE recorded within bulk carbonate from the CIE core interval varies by depth in the Marlboro Clay, with more negative $\delta^{13}C$ values nearshore than offshore, although the magnitude of the CIE recorded in benthic foraminifera shows little to no deviation (Bralower et al., 2018; John et al., 2008; Kent et al., 2003; Self-Trail et al., 2012, 2017; Stassen et al., 2012; Zachos et al., 2006). This off-shore gradient has been variably attributed to differences in coastal marine productivity (Gibbs et al., 2006; John et al., 2008; Stassen et al., 2012), sediment reworking (John et al., 2008; Stassen et al., 2012), cometary debris (Kent et al., 2003), or as an artifact of authigenic siderite (Bralower et al., 2018; Self-Trail et al., 2017). This last interpretation is supported by clast counts and clast morphology of siderite in washed samples of PETM sediments from the Maryland and New Jersey coast (Bralower et al., 2018; Self-Trail et al., 2017), including sediments from the Wilson Lake-A core (Bralower et al., 2018) that have been the focus of several of our studies on magnetofossils (Lippert & Zachos, 2007; Wagner, Egli, et al., 2021; Wagner, Lascu, et al., 2021).

Siderite ($FeCO_3$) is a common diagenetic carbonate in iron and carbon-rich marine sediments (Ellwood et al., 1986, 1988; Vuillemin et al., 2019). Paleomagnetically, iron-rich carbonates can be problematic because they can quickly oxidize to magnetite, maghemite, or hematite with little or no heating and produce aberrant remanence directions and secondary nanoparticles of magnetite (Ellwood et al., 1986, 1988; Golden et al., 2004). Although siderite carries no remanence at room temperature (RT), it is antiferromagnetic below 37 K. Thus, it can be detected in bulk sediments using Field-Cooled (FC) and Zero-Field Cooled (ZFC) remanence experiments (Bilardello & Jackson, 2013; Housen et al., 1996; Pan et al., 2002).

A principal goal for my fellowship was to understand the composition and remanence characteristics of the PETM magnetofossil assemblage from the Wilson Lake-A core. I also wanted to test if I could use non-destructive low temperature (LT) remanence measurements to assess the presence and relative abundance of siderite in these bulk samples. This approach allows me to directly compare the interpretations regarding siderite to our previous work distinguishing and quantifying morphologically distinct magnetofossil assemblages (Wagner, Lascu, et al., 2021).

Seventeen samples were selected from the Wilson Lake-A core that span four of the six PETM intervals: the pre-CIE, CIE onset, CIE core, and post-CIE intervals. The Wilson Lake-A core does not record either of the CIE recovery intervals. I measured the FC and ZFC LT saturation remanent magnetization (SIRM) and the LT demagnetization of RT SIRM of each of these samples using the Magnetic Properties Measurement System instruments at the Institute for Rock Magnetism (IRM). I then normalized the FC-ZFC-RT data for each specimen to the initial FC remanence. The derivatives of the FC and ZFC curves are shown here to better observe the LT remanence behavior in the samples, such as phase transitions like the Verwey transition (T_V) for magnetite (e.g., Stacey & Banerjee, 1974), the double TV which distinguishes abiotic from biotic magnetite (Chang et al., 2016), and the Néel temperature for siderite (Jacobs, 1963).

The FC-ZFC-RT datasets from each of the four PETM intervals at Wilson Lake show little to no variation within each stratigraphic interval (i.e., pre-CIE, CIE onset, CIE core, and post-CIE intervals). Therefore, I focus on the variation, and similarities, observed between the intervals in the descriptions below using a representative sample from each of the four intervals (Figure).

Verwey transitions (T_V) are observed between ~90-120 K in each of the PETM intervals, indicating that magnetite is present within each of the samples (Figure). There is a weak double TV transition in the FC curves from the CIE onset interval, further suggesting mixtures of detrital and biogenic magnetite (Chang et al., 2016). This is consistent with our published RT measurements

and electron microscopy (Lippert & Zachos, 2007; Wagner, Egli, et al., 2021; Wagner, Lascu, et al., 2021). A more thorough investigation of the different populations of magnetite as revealed by these LT measurements is discussed in a separate publication in preparation.

The LT remanence of specimens representing the CIE onset and core intervals show at least one other LT inflection between 25-30 K in the FC and ZFC curves (Figure). Although the FC and ZFC curves from both the pre- and post-CIE intervals do not show as clear an inflection over this temperature range, the remanence of both sets of curves decreases rapidly with warming over this range. Siderite was documented in smear slides from the Wilson Lake-A core (Bralower et al., 2018), so I conclude that this LT behavior is due to warming through the Néel temperature for siderite (Housen et al., 1996; Jacobs, 1963).

The LT data suggest that siderite is more abundant and well-mineralized within the CIE core interval at Wilson Lake: I interpret this from the muted magnetite signatures and sharper transitions at the Néel temperature within this interval (Figure). This interpreted increase in siderite content is corroborated by a separate study that reports a small, concomitant increase in siderite grains and more negative carbon isotope values from the low carbonate interval (approximately equivalent to the CIE onset interval) to the non-low carbonate interval (roughly equivalent to the CIE core interval) in the Wilson Lake-A core (Bralower et al., 2018). I note that the LT remanence data from the CIE core interval samples are very similar to FC, ZFC, and RT cycling datasets for modern samples known to contain siderite (Abdulkarim, 2020). A more thorough description and discussion of the implications of this siderite for magnetofossil and environmental interpretations is forthcoming in another publication.

Identification of different iron mineral phases is important for understanding the depositional, diagenetic, and authigenic processes in sediments that underly our interpretation of climatic and ecological events in the geologic record. The LT remanence measurements confirm the presence of siderite at Wilson Lake-A (Bralower et al., 2018), underscoring the capability of these measurements to detect iron minerals that otherwise elude RT measurements like first-order reversal curve measurements (Wagner, Lascu, et al., 2021).

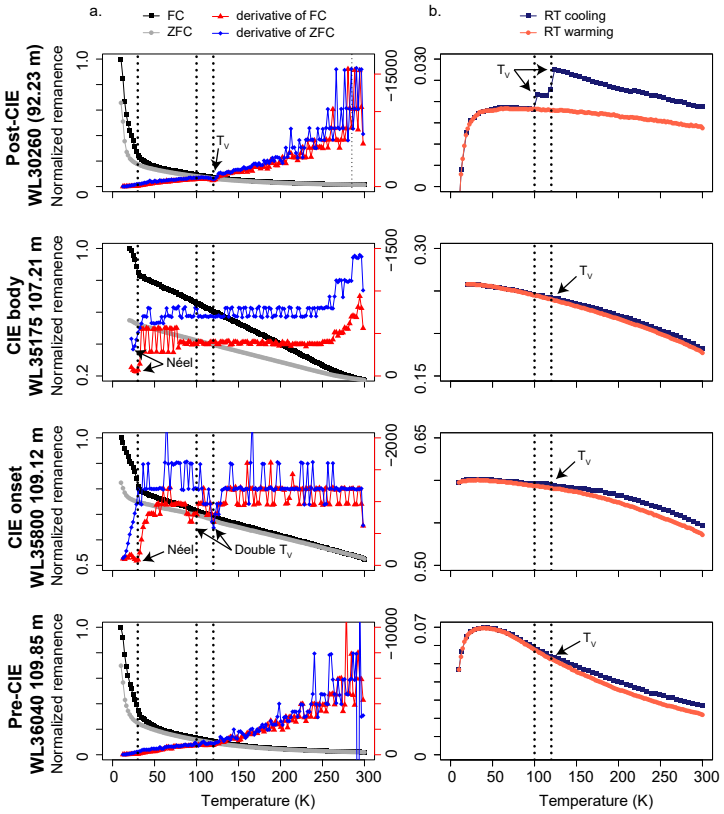

Figure. Low temperature remanence results from four representative stratigraphic intervals from the PETM at Wilson Lake-A. Rows: The four stratigraphic intervals are: the pre-CIE, CIE onset, CIE core, and post-CIE intervals. Columns: (a) Normalized FC and ZFC LT-SIRM curves (black and gray curves) with derivatives (red and blue curves). The three dotted vertical lines mark 30, 100, and 120 K. These temperatures correspond to the interpreted phase transitions for siderite, oxidized or biogenic magnetite, and unoxidized magnetite (Chang et al., 2016; Housen et al., 1996; Stacey & Banerjee, 1974), respectively. Low temperature features that correspond to these transitions are indicated by arrows (e.g., "Néel" for siderite, "T_V" for magnetite, and "Double T_V" for both abiotic and biogenic magnetite transitions). (b) Normalized RT-SIRM cycling curves (blue is cooling, red is warming). Similar to (a), the two dotted vertical lines mark 100 and 120 K, or the two T_V's for magnetite; features corresponding to these transitions are also indicated with arrows. I interpret the pronounced T_V's from the post-CIE interval to physical grain movement during the measurement.

Acknowledgements

I would like to thank the IRM staff including Mike Jackson, Peat Solheid, Dario Bilardello, Bruce Moskowitz, and Josh Feinberg for their advice, expertise, and constructive conversations. I am very grateful for the funding support for this IRM Visiting Fellowship to collect these LT datasets. IRM Visiting Fellowships are supported in part by NSF grants awarded to the IRM.

References

Abdulkarim. (2020). Testing the universality and scale of the magnetic hydrocardbon migration hypothesis-Catcher Area Development, Western shelf, UK North Sea. 30(4), 2–3.

Bilardello, D., & Jackson, M. (2013). What do the Mumpsies do? IRM Quarterly, 23(3), 1–16.

Bralower, T. J., Kump, L. R., Self-Trail, J. M., Robinson, M. M., Lyons, S., Babila, T., Ballaron, E., Freeman, K. H., Hajek, E., Rush, W., & Zachos, J. C. (2018). Evidence for Shelf Acidification During the Onset of the Paleocene-Eocene Thermal Maximum. Paleoceanography and Paleoclimatology, 33(12), 1408–1426. https://doi.org/10.1029/2018PA003382

Chang, L., Heslop, D., Roberts, A. P., Rey, D., & Mohamed, K. J. (2016). Discrimination of biogenic and detrital magnetite through a double Verway transition temperature. Journal of Geophysical Research : Solid Earth, 121(1), 3–14. https://doi.org/10.1002/2014JB011237.Received

Ellwood, B. B., Balsam, W., Burkart, B., Long, G. J., & Buhl, M. L. (1986). Anomalous magnetic properties in rocks containing the mineral siderite: Paleomagnetic implications. Journal of Geophysical Research: Solid Earth, 91(B12), 12779–12790. https://doi.org/10.1029/jb091ib12p12779

Ellwood, B. B., Chrzanowski, T. H., Hrouda, F., Long, G. J., & Buhl, M. L. (1988). Siderite formation in anoxic deep-sea sediments: a synergetic bacterially controlled

process with important implications in paleomagnetism. Geology, 16(11), 980–982. https://doi.org/10.1130/0091-7613(1988)016<0980:SFIADS>2.3.CO

Gibbs, S. J., Bralower, T. J., Bown, P. R., Zachos, J. C., & Bybell, L. M. (2006). Shelf and open-ocean calcareous phytoplankton assemblages across the Paleocene-Eocene thermal maximum: Implications for global productivity gradients. Geology, 34(4), 233–236. https://doi.org/10.1130/G22381.1

Golden, D. C., Ming, D. W., Morris, R. V., Brearley, A. J., Lauer, H. V., Treiman, A. H., Zolensky, M. E., Schwandt, C. S., Lofgren, G. E., & McKay, G. A. (2004). Evidence for exclusively inorganic formation of magnetite in Martian meteorite ALH84001. American Mineralogist, 89(5–6), 681–695. https://doi.org/10.2138/am-2004-5-602

Housen, B. A., Banerjee, S. K., & Moskowitz, B. M. (1996). Low temperature magnetic properties of siderite and magnetite in marine sediments. Geophysical Research Letters, 23(20), 2843–2846. https://doi.org/10.1029/96GL01197

Jacobs, I. S. (1963). Metamagnetism of siderite (FeCO3). Journal of Applied Physics, 34(4), 1106–1107. https://doi.org/10.1063/1.1729389

John, C. M., Bohaty, S. M., Zachos, J. C., Sluijs, A., Gibbs, S., Brinkhuis, H., & Bralower, T. J. (2008). North American continental margin records of the Paleocene-Eocene thermal maximum: Implications for global carbon and hydrological cycling. Paleoceanography, 23(2), 1–20. https://doi.org/10.1029/2007PA001465

Kennett, J. P., & Stott, L. D. (1991). Abrupt deep sea warming, paleoceanographic changes and benthic extinctions at the end of the Paleocene. Nature, 353(6341), 225–229. https://doi.org/10.1038/353225a0

Kent, D. V., Cramer, B. S., Lanci, L., Wang, D., Wright, J. D., & Van der Voo, R. (2003). A case for a comet impact trigger for the Paleocene/Eocene thermal maximum and carbon isotope excursion. Earth and Planetary Science Letters, 211(1–2), 13–26. https://doi.org/10.1016/S0012-821X(03)00188-2

Lippert, P. C., & Zachos, J. C. (2007). A biogenic origin for anomalous fine-grained magnetic material at the Paleocone-Eocene boundary at Wilson Lake, New Jersey. Paleoceanography, 22(4), PA4104 1-8. https://doi.org/10.1029/2007PA001471

McInerney, F. A., & Wing, S. L. (2011). The Paleocene-Eocene Thermal Maximum: A perturbation of carbon cycle, climate, and biosphere with implications for the future. Annual Review of Earth and Planetary Sciences, 39(1), 489–516. https://doi.org/10.1146/annurev-earth-040610-133431

Pan, Y., Zhu, R., Liu, Q., & Jackson, M. (2002). Low-temperature magnetic behavior related to thermal alteration of siderite. Geophysical Research Letters, 29(23), 2-1-2–4. https://doi.org/10.1029/2002GL016021

Self-Trail, J. M., Powars, D. S., Watkins, D. K., & Wandless, G. A. (2012). Calcareous nannofossil assemblage changes across the Paleocene-Eocene Thermal Maximum: Evidence from a shelf setting. Marine Micropaleontology, 92–93, 61–80. https://doi.org/10.1016/j.marmicro.2012.05.003

Self-Trail, J. M., Robinson, M. M., Bralower, T. J., Sessa, J. A., Hajek, E. A., Kump, L. R., Trampush, S. M., Willard, D. A., Edwards, L. E., Powars, D. S., & Wandless, G. A. (2017). Shallow marine response to global climate change during the Paleocene-Eocene Thermal Maximum, Salisbury Embayment, USA. Paleoceanography, 32(7), 710–728. https://doi.org/10.1002/2017PA003096

Stacey, F. D., and S. K. Banerjee (1974), The Physical Principles of Rock Magnetism, Elsevier Scientific Publ. Company, Amsterdam

Stassen, P., Thomas, E., & Speijer, R. P. R. P. (2012). Integrated stratigraphy of the Paleocene-Eocene Thermal Maximum in the New Jersey Coastal Plain: Toward understanding the effects of global warming in a shelf environment. Paleoceanography, 27(4), 1–17. https://doi.org/10.1029/2012PA002323

Thomas, E., & Shackleton, N. J. (1996). The Paleocene-Eocene benthic foraminiferal extinction and stable isotope anomalies. Geological Society, London, Special Publications, 101(1), 401–441. https://doi.org/10.1144/GSL.SP.1996.101.01.20

Vuillemin, A., Wirth, R., Kemnitz, H., Schleicher, A. M., Friese, A., Bauer, K. W., Simister, R., Nomosatryo, S., Ordoñez, L., Ariztegui, D., Henny, C., Crowe, S. A., Benning, L. G., Kallmeyer, J., Russell, J. M., Bijaksana, S., Vogel, H., & Towuti Drilling Project Science Team, the. (2019). Formation of diagenetic siderite in modern ferruginous sediments. Geology, 47(6), 540–544. https://doi.org/10.1130/G46100.1

Wagner, C. L., Egli, R., Lascu, I., Lippert, P. C., Livi, K. J. T., & Sears, H. B. (2021). In-situ magnetic identification of giant, needle-shaped magnetofossils in Paleocene-Eocene Thermal Maximum sediments. Proceedings of the National Academy of Sciences, 118(6), e2018169118. https://doi.org/10.1073/pnas.2018169118

Wagner, C. L., Lascu, I., Lippert, P. C., Egli, R., Livi, K. J. T. T., & Sears, H. B. (2021). Diversification of iron-biomineralizing organisms during the Paleocene-Eocene Thermal Maximum: Evidence from quantitative unmixing of conventional and giant magnetofossils. Paleoceanography and Paleoclimatology, 36(5), 1-25 e2021PA004225. https://doi.org/10.1029/2021PA004225

Westerhold, T., Marwan, N., Drury, A. J., Liebrand, D., Agnini, C., Anagnostou, E., Barnet, J. S. K., Bohaty, S. M., De Vleeschouwer, D., Florindo, F., Frederichs, T., Hodell, D. A., Holbourn, A. E., Kroon, D., Lauretano, V., Littler, K., Lourens, L. J., Lyle, M., Pälike, H., … Zachos, J. C. (2020). An astronomically dated record of Earth's climate and its predictability over the last 66 million years. Science, 369(6509), 1383–1388. https://doi.org/10.1126/SCIENCE.ABA6853

Westerhold, T., Röhl, U., Wilkens, R. H., Gingerich, P. D., Clyde, W. C., Wing, S. L., Bowen, G. J., & Kraus, M. J. (2018). Synchronizing early Eocene deep-sea and continental records - Cyclostratigraphic age models for the Bighorn Basin Coring Project drill cores. Climate of the Past, 14(3), 303–319. https://doi.org/10.5194/cp-14-303-2018

Zachos, J. C., Schouten, S., Bohaty, S., Quattlebaum, T., Sluijs, A., Brinkhuis, H., Gibbs, S. J. J., & Bralower, T. J. J. (2006). Extreme warming of mid-latitude coastal ocean during the Paleocene-Eocene Thermal Maximum: Inferences from TEX86 and isotope data. Geology, 34(9), 737. https://doi.org/10.1130/G22522.1

Zeebe, R. E., Ridgwell, A., & Zachos, J. C. (2016). Anthropogenic carbon release rate unprecedented during the past 66 million years. Nature Geoscience, 9(4), 325–329. https://doi.org/10.1038/ngeo2681

Current Articles

A list of current research articles dealing with various topics in the physics and chemistry of magnetism is a regular feature of the IRM Quarterly. Articles published in familiar geology and geophysics journals are included; special emphasis is given to current articles from physics, chemistry, and materials-science journals. Most are taken from ISI Web of Knowledge, after which they are subjected to Procrustean culling for this newsletter. An extensive reference list of articles (primarily about rock magnetism, the physics and chemistry of magnetism, and some paleomagnetism) is continually updated at the IRM. This list, with more than 10,000 references, is available free of charge. Your contributions both to the list and to the Current Articles section of the IRM Quarterly are always welcome.

Environmental Magnetism

Amor, M., J. Wan, R. Egli, J. Carlut, C. Gatel, I. M. Andersen, E. Snoeck, and A. Komeili (2022), Key Signatures of Magnetofossils Elucidated by Mutant Magnetotactic Bacteria and Micromagnetic Calculations, Journal of Geophysical Research-Solid Earth, 127(1), doi:10.1029/2021jb023239.

Badesab, F., V. Gaikwad, M. Venkateshwarlu, N. Kadam, and H. M. Joao (2022), Diagenetic dissolution, maghemitization and sulphidization of magnetic minerals in rapidly deposited gas hydrate bearing sediments from the Bay of Bengal, Marine and Petroleum Geology, 139, doi:10.1016/j.marpetgeo.2022.105585.

Chen, Q., X. M. Liu, G. Y. Zhao, J. Jia, W. Ye, B. Lu, M. Meadows, and J. Q. Guan (2022), 0.2 Ma or 1.2 Ma? Timing of the Linking of the Middle and Lower Reaches of the Yellow River Inferred From Loess-Palaeosol Sequences, Geophysical Research Letters, 49(6), doi:10.1029/2021gl097510.

de Mello, D. C., et al. (2022), A new methodological framework for geophysical sensor combinations associated with machine learning algorithms to understand soil attributes, Geoscientific Model Development, 15(3), 1219-1246, doi:10.5194/gmd-15-1219-2022.

Delusina, I., S. W. Starratt, and K. L. Verosub (2022), Environmental evolution of peat in the Sacramento - San Joaquin Delta (California) during the Middle and Late Holocene as deduced from pollen, diatoms and magnetism, Quaternary International, 621, 50-61, doi:10.1016/j.quaint.2020.05.012.

Dong, H. M., Y. G. Song, L. M. Chen, H. F. Liu, X. F. Fu, and M. P. Xie (2022), Soil erosion and human activities over the last 60 years revealed by magnetism, particle size and minerals of check dams sediments on the Chinese Loess Plateau, Environmental Earth Sciences, 81(5), doi:10.1007/s12665-022-10245-8.

Fan, J. W., H. Y. Xu, W. Shi, Q. Q. Guo, S. Q. Zhang, X. T. Wei, M. G. Cai, S. T. Huang, J. Y. Wang, and J. L. Xiao (2022), A similar to 28-kyr Continuous Lacustrine Paleoseismic Record of the Intraplate, Slow-Slipping Fuyun Fault in Northwest China, Frontiers in Earth Science, 10, doi:10.3389/feart.2022.828801.

Gao, P., J. S. Nie, D. O. Breecker, T. Gallagher, L. Serach, and A. M. Alonso-Zarza (2022), Similar Magnetic Enhancement Mechanisms Between Chinese Loess and Alluvial Sediments From the Teruel Basin, NE Spain, and Paleoclimate Implications, Geophysical Research Letters, 49(6), doi:10.1029/2021gl096977.

Gorbarenko, S., and G. Malakhova (2021), Orbital and suborbital environmental changes in the Western Bering Sea during the last 172 ka Inferred from Diatom and Productivity Proxies, Global and Planetary Change, 198, doi:10.1016/j.gloplacha.2020.103405.

Hoffmann, N., G. Tortella, E. Hermosilla, P. Fincheira, M. C. Diez, I. M. Lourenco, A. B. Seabra, and O. Rubilar (2022), Comparative Toxicity Assessment of Eco-Friendly Synthesized Superparamagnetic Iron Oxide Nanoparticles (SPIONs) in Plants and Aquatic Model Organisms, Minerals, 12(4), doi:10.3390/min12040451.

Jiang, H., J. Zhang, S. Zhang, N. Zhong, S. Wan, G. I. Alsop, H. Xu, Q. Guo, and Z. Yan (2022a), Tectonic and Climatic Impacts on Environmental Evolution in East Asia During the Palaeogene, Geophysical Research Letters, 49(3), doi:10.1029/2021gl096832.

Jiang, X. D., et al. (2022b), Abyssal Manganese Nodule Recording of Global Cooling and Tibetan Plateau Uplift Impacts on Asian Aridification, Geophysical Research Letters, 49(3), doi:10.1029/2021gl096624.

Li, P., C. X. Zhang, H. B. Wu, and Z. W. Gao (2022), Geochemical characteristics of Holocene loess-paleosol sequences in central Chinese Loess Plateau and their implications for East Asian monsoon evolution, Quaternary International, 616, 99-108, doi:10.1016/j.quaint.2021.10.017.

Lian, Y. C., X. M. Liu, A. R. Tabrez, X. G. Mao, M. M. Ma, X. Y. Qi, and S. F. Zhou (2022), The magnetic properties of Attock loess and its environmental significance in Pakistan, Quaternary International, 616, 120-132, doi:10.1016/j.quaint.2021.11.011.

Liu, X. K., R. J. Lu, Z. Y. Ding, Z. Lyu, Y. J. Li, and Z. B. Dong (2021), Holocene Environmental Changes Inferred From an Aeolian-Palaeosol-Lacustrine Profile in the Mu Us Desert, Northern China, Frontiers in Earth Science, 9, doi:10.3389/feart.2021.799935.

Oestreicher, Z., L. Perez-Guzman, N. N. Casillas-Ituarte, M. R. Hostetler, E. Mumper, D. A. Bazylinski, S. K. Lower, and B. H. Lower (2022), Thermophilic Magnetotactic Bacteria from Mickey Hot Springs, an Arsenic-Rich Hydrothermal System in Oregon, Acs Earth and Space Chemistry, 6(3), 530-540, doi:10.1021/acsearthspacechem.1c00318.

Ohenhen, L. O., J. M. Feinberg, L. D. Slater, D. Ntarlagiannis, I. M. Cozzarelli, M. Rios-Sanchez, C. W. Isaacson, A. Stricker, and E. A. Atekwana (2022), Microbially Induced Anaerobic Oxidation of Magnetite to Maghemite in a Hydrocarbon-Contaminated Aquifer, Journal of Geophysical Research-Biogeosciences, 127(4), doi:10.1029/2021jg006560.

Qin, J., R. Zhang, V. A. Kravchinsky, J. P. Valet, L. Sagnotti, J. X. Li, Y. Xu, T. Anwar, and L. P. Yue (2022), 1.2 Myr Band of Earth-Mars Obliquity Modulation on the Evolution of Cold Late Miocene to Warm Early Pliocene Climate, Journal of Geophysical Research-Solid Earth, 127(4), doi:10.1029/2022jb024131.

Rasooli, N., M. Mahmoodabadi, M. H. Farpoor, and I. E. Boroujeni (2022), Pedoenvironmental variations assessment using magnetic susceptibility in Lut Watershed, Central Iran, Journal of Applied Geophysics, 198, doi:10.1016/j.jappgeo.2022.104582.

Roy, I., N. Tomar, M. Shekhar, S. Agrawal, A. Bhattacharyya, P. Kumar, R. Sharma, P. S. Ranhotra, and S. K. Patil (2022), Reconstruction of the late Holocene climate variability from the summer monsoon dominated Bhagirathi valley, western Himalaya, Journal of Asian Earth Sciences, 227, doi:10.1016/j.jseaes.2022.105080.

Sassi, M., and K. M. Rosso (2022), Ab Initio Evaluation of Solid-State Transformation Pathways from Ferrihydrite to Goethite, Acs Earth and Space Chemistry, 6(3), 800-809, doi:10.1021/acsearthspacechem.2c00026.

Sheikh, H. A., B. A. Maher, V. Karloukovski, G. I. Lam-

pronti, and R. J. Harrison (2022), Biomagnetic Characterization of Air Pollution Particulates in Lahore, Pakistan, Geochemistry Geophysics Geosystems, 23(2), doi:10.1029/2021gc010293.

Staley, S. E., P. J. Fawcett, R. S. Anderson, and G. Jimenez-Moreno (2022), Early Pleistocene-to-present paleoclimate archive for the American Southwest from Stoneman Lake, Arizona, USA, Geological Society of America Bulletin, 134(3-4), 791-814, doi:10.1130/b36038.1.

Su, B., J. M. Sun, and C. S. Jin (2022), Orbital Forcing of Climatic Changes on the Central Tibetan Plateau Reveals Late Oligocene to Early Miocene South Asian Monsoon Evolution, Geophysical Research Letters, 49(5), doi:10.1029/2021gl097428.

Tauseef, M., E. Ray, D. Paul, J. N. Malik, and I. Ahmad (2022), Mineralogical, geochemical, and magnetic susceptibility variations in the loess-paleosol sequence from Pattan, Kashmir Valley, India record an enhanced Indian summer monsoon around 35 ka, Quaternary International, 616, 55-66, doi:10.1016/j.quaint.2021.12.014.

Timireva, S. N., Y. M. Kononov, S. A. Sycheva, N. A. Taratunina, P. I. Kalinin, K. P. Filippova, A. L. Zakharov, E. A. Konstantinov, A. S. Murray, and R. N. Kurbanov (2022), Revisiting the Taman peninsula loess-paleosol sequence: Middle and Late Pleistocene record of Cape Pekla, Quaternary International, 620, 36-45, doi:10.1016/j.quaint.2021.06.010.

Wang, P. C., T. H. Shi, N. Mehta, S. S. Yang, H. M. Wang, D. Liu, and Z. M. Zhu (2022), Changes in Magnetic Properties of Magnetite Nanoparticles Upon Microbial Iron Reduction, Geochemistry Geophysics Geosystems, 23(3), doi:10.1029/2021gc010212.

Xu, C. X., C. Y. E, Y. K. Shi, J. Zhang, M. P. Sun, Z. K. Zhang, and Y. X. Zeng (2022), Holocene Aeolian Activity Recorded by Mountain Paleosols, Gonghe Basin, Northeast Qinghai-Tibet Plateau, Frontiers in Earth Science, 10, doi:10.3389/feart.2022.832993.

Xue, P. F., L. Chang, Z. W. Pei, and R. J. Harrison (2022), Discovery of giant magnetofossils within and outside of the Palaeocene-Eocene Thermal Maximum in the North Atlantic, Earth and Planetary Science Letters, 584, doi:10.1016/j.epsl.2022.117417.

Yang, L. J., L. J. Wu, R. Zhang, and B. B. Ye (2022), Grain size characteristics of borehole sediments from Xinji Area, Hebei Plain and their implications on sedimentary environment, Arabian Journal of Geosciences, 15(4), doi:10.1007/s12517-022-09474-9.

Yang, S. L., Z. X. Chen, H. Chen, Y. L. Luo, L. Liu, X. J. Liu, Q. Li, J. T. Zhou, and P. S. Li (2022), Magnetic Properties of the Ganzi Loess and Their Implications for Precipitation History in the Eastern Tibetan Plateau Since the Last Interglacial, Paleoceanography and Paleoclimatology, 37(2), doi:10.1029/2021pa004322.

Extraterrestrial and Planetary Magnetism

Sinha, P., and B. Horgan (2022), Sediments Within the Icy North Polar Deposits of Mars Record Recent Impacts and Volcanism, Geophysical Research Letters, 49(8), doi:10.1029/2022gl097758.

Suttle, M. D., A. J. King, N. K. Ramkissoon, E. Bonato, I. A. Franchi, J. Malley, P. F. Schofield, J. Najorka, T. Salge, and S. S. Russell (2022), Alteration conditions on the CM and CV parent bodies - Insights from hydrothermal experiments with the CO chondrite Kainsaz, Geochimica Et Cosmochimica Acta, 318, 83-111, doi:10.1016/j.gca.2021.11.028.

Fundamental Rock Magnetism and applications

Dias, J. M., C. Cruz, H. Sant'Ovaia, and F. Noronha (2022), Assessing the Magnetic Mineralogy of the Pre-Variscan Manteigas Granodiorite: An Unexpected Case of a Magnetite-Series Granitoid in Portugal, Minerals, 12(4), doi:10.3390/min12040440.

Gehring, A. U., A. Firlus, D. Koulialias, P. G. Weidler, and J. F. Loffler (2021), The Besnus transition in 4C pyrrhotite revisited, Geophysical Journal International, 228(3), 1724-1730, doi:10.1093/gji/ggab430.

Jiang, Z. X., Q. S. Liu, A. P. Roberts, M. J. Dekkers, V. Barron, J. Torrent, and S. Z. Li (2022), The Magnetic and Color Reflectance Properties of Hematite: From Earth to Mars, Reviews of Geophysics, 60(1), doi:10.1029/2020rg000698.

Kanamaru, T., K. Furukawa, X. Y. Zhao, and Y. Suganuma (2022), Magnetic petrology of pumice fall deposits of the 1783 eruption of Asama volcano, Japan, Earth Planets and Space, 74(1), doi:10.1186/s40623-022-01618-1.

Khanna, T. C., and K. Arora (2022), Elusive origin of the subsurface tephra in the Deccan volcanic province, India, Journal of Earth System Science, 131(1), doi:10.1007/s12040-021-01786-w.

Kozhevnikov, N. O., and E. Y. Antonov (2022), Aftereffects in the Transient Electromagnetic Method: Magnetic Viscosity, Russian Geology and Geophysics, 63(3), 312-320, doi:10.2113/RGG20204306GeologiyaiGeofizika.

Lerner, G. A., E. J. Piispa, J. A. Bowles, and M. H. Ort (2022), Paleomagnetism and rock magnetism as tools for volcanology, Bulletin of Volcanology, 84(3), doi:10.1007/s00445-022-01529-9.

Nikolaisen, E. S., R. Harrison, K. Fabian, N. Church, S. A. McEnroe, B. E. Sorensen, and C. Tegner (2022), Hysteresis parameters and magnetic anisotropy of silicate-hosted magnetite exsolutions, Geophysical Journal International, 229(3), 1695-1717, doi:10.1093/gji/ggac007.

Out, F., D. Cortes-Ortuno, K. Fabian, T. van Leeuwen, and L. V. de Groot (2022), A First-Order Statistical Exploration of the Mathematical Limits of Micromagnetic Tomography, Geochemistry Geophysics Geosystems, 23(4), doi:10.1029/2021gc010184.

Pei, Z. W., T. A. Berndt, L. Chang, F. Bai, W. Williams, and G. A. Paterson (2022), Bending and Collapse: Magnetic Recording Fidelity of Magnetofossils From Micromagnetic Simulation, Journal of Geophysical Research-Solid Earth, 127(4), doi:10.1029/2021jb023447.

Roberts, A. P., et al. (2021), Magnetic Domain State and Anisotropy in Hematite (alpha-Fe2O3) From First-Order Reversal Curve Diagrams, Journal of Geophysical Research-Solid Earth, 126(12), doi:10.1029/2021jb023027.

Slay, D., Cao, D., Ferré, E. C., and M. Charilaou (2021), Ferromagnetic resonance of superparamagnetic nanoparticles: The effect of dipole–dipole interactions, J. Appl. Phys. 130, 113902, doi: 10.1063/5.0060769.

Wang, S. S., L. Chang, C. H. Tao, D. Bilardello, L. Liu, and T. Wu (2021), Seafloor Magnetism Under Hydrothermal Alteration: Insights From Magnetomineralogy and Magnetic Properties of the Southwest Indian Ridge Basalts, Journal of Geophysical Research-Solid Earth, 126(12), doi:10.1029/2021jb022646.

Geomagnetism, Paleointensity and Records of the Geomagnetic Field

Biasi, J., J. L. Kirschvink, and R. R. Fu (2021), Characterizing the Geomagnetic Field at High Southern Latitudes: Evidence From the Antarctic Peninsula, Journal of Geophysical Research-Solid Earth, 126(12), doi:10.1029/2021jb023273.

Bobrovnikova, E. M., F. Lhuillier, V. P. Shcherbakov, V. V. Shcherbakova, G. V. Zhidkov, I. E. Lebedev, B. Eid, and V. E. Pavlov (2022), High-Latitude Paleointensities During the Cretaceous Normal Superchron From the Okhotsk-Chukotka Volcanic Belt, Journal of Geophysical Research-Solid Earth, 127(2), doi:10.1029/2021jb023551.

Bono, R. K., et al. (2022), The PINT database: a definitive compilation of absolute palaeomagnetic intensity determinations since 4 billion years ago, Geophysical Journal International, 229(1), 522-545, doi:10.1093/gji/ggab490.

Buffett, B. A., M. S. Avery, and W. Davis (2022), A Physical Interpretation of Asymmetric Growth and Decay of the Geomagnetic Dipole Moment, Geochemistry Geophysics Geosystems, 23(3), doi:10.1029/2021gc010239.

Davis, W., and B. Buffett (2021), Inferring core processes using stochastic models of the geodynamo, Geophysical Journal International, 228(3), 1478-1493, doi:10.1093/gji/ggab412.

Di Chiara, A., and F. J. Pavon-Carrasco (2022), A first regional model of the past Earth's magnetic field from Africa for the last 4000 years, Physics of the Earth and Planetary Interiors, 325, doi:10.1016/j.pepi.2022.106855.

Eid, B., F. Lhuillier, V. P. Shcherbakov, and V. V. Shcherbakova (2022), Do changes in geomagnetic secular variation, dipole moment and polarity reversal frequency correlate over the past 155 Myr?, Geophysical Journal International, 230(2), 1132-1146, doi:10.1093/gji/ggac112.

Eliseev, A. A., V. V. Shcherbakova, D. V. Metelkin, N. E. Mikhaltsov, G. V. Zhidkov, V. V. Abashev, and A. M. Rogov (2022), Low Geomagnetic Field Paleointensity on the Permian-Triassic Boundary from Study of the Kuznetsk Basin Traps (Southern Siberia), Russian Geology and Geophysics, 63(2), 193-207, doi:10.2113/rgg20204330.

Gao, J. W., M. Korte, S. Panovska, Z. J. Rong, and Y. Wei (2022), Effects of the Laschamps Excursion on Geomagnetic Cutoff Rigidities, Geochemistry Geophysics Geosystems, 23(2), doi:10.1029/2021gc010261.

Gong, F., Y. Q. Yu, J. B. Cao, Y. Wei, J. W. Gao, H. Li, B. Z. Zhang, and A. Ridley (2022), Simulating the Solar Wind-Magnetosphere Interaction During the Matuyama-Brunhes Paleomagnetic Reversal, Geophysical Research Letters, 49(3), doi:10.1029/2021gl097340.

Hyodo, M., et al. (2022), Intermittent non-axial dipolar-field dominance of twin Laschamp excursions, Communications Earth & Environment, 3(1), doi:10.1038/s43247-022-00401-0.

Lebedev, I. E., E. M. Bobrovnikova, P. L. Tikhomirov, B. Eid, F. Lhuillier, and V. E. Pavlov (2022), Amplitude of Secular Geomagnetic Variation in Late Cretaceous Based on Paleomagnetic Studies of the Okhotsk-Chukotka Volcanic Belt from Upper Reaches of Malyi Anyui River, West Chukotka, Izvestiya-Physics of the Solid Earth, 58(2), 185-202, doi:10.1134/s1069351322020045.

Maffione M., and E. Herrero-Bervera (2022), A Relative Paleointensity (RPI)- Calibrated Age Model for the Corinth Syn-rift Sequence at IODP Hole M0079A (Gulf of Corinth, Greece). Frontiers in Earth Sciences, 10:813958, doi: 10.3389/feart.2022.813958.

Maksimochkin, V. I., R. A. Grachev, and A. N. Tselebrovskiy (2022), Effect of Single-Phase Oxidation of Titanomagnetite in Basalts on the Determination of Intensity and Direction of Paleomagnetic Field, Izvestiya-Physics of the Solid Earth, 58(2), 216-229, doi:10.1134/s1069351322020070.

Panovska, S., M. Korte, J. B. Liu, and N. Nowaczyk (2021), Global Evolution and Dynamics of the Geomagnetic Field in the 15-70 kyr Period Based on Selected Paleomagnetic Sediment Records, Journal of Geophysical Research-Solid Earth, 126(12), doi:10.1029/2021jb022681.

Velle, J. H., M. H. Walczak, B. Reilly, G. St-Onge, J. S. Stoner, S. Fallon, A. C. Mix, C. Belanger, and M. Forwick (2021), High resolution inclination records from the Gulf of Alaska, IODP Expedition 341 Sites U1418 and U1419, Geophysical Journal International, 229(1), 345-358, doi:10.1093/gji/ggab479.

Yamamoto, Y., L. Tauxe, H. Ahn, and C. Santos (2022), Absolute Paleointensity Experiments on Aged Thermoremanent Magnetization: Assessment of Reliability of the Tsunakawa-Shaw and Other Methods With Implications for "Fragile" Curvature, Geochemistry Geophysics Geosystems, 23(4), doi:10.1029/2022gc010391.

Yang, X. Q., T. W. Zhang, E. Zhang, J. Toney, Q. X. Zhou, and Y. X. Xie (2022), Paleosecular Variations During the Last Glacial Period From Tengchong Qinghai Lake, Yunnan Province, China, Journal of Geophysical Research-Solid Earth, 127(3), doi:10.1029/2021jb023459.

Yoshimura, Y. (2022), The Cretaceous Normal Superchron: A Mini-Review of Its Discovery, Short Reversal Events, Paleointensity, Paleosecular Variations, Paleoenvironment, Volcanism, and Mechanism, Frontiers in Earth Science, 10, doi:10.3389/feart.2022.834024.

Magnetic Fabrics and Anisotropy

Ageeva, O., G. Habler, S. A. Gilder, R. Schuster, A. Pertsev, O. Pilipenko, G. Bian, and R. Abart (2022), Oriented Magnetite Inclusions in Plagioclase: Implications for the Anisotropy of Magnetic Remanence, Geochemistry Geophysics Geosystems, 23(2), doi:10.1029/2021gc010272.

Assis, O. S., C. B. Zaffarana, D. Orts, C. Puigdomenech, V. R. Gonzalez, G. Gallastegui, N. Hauser, E. S. Kiseeva, J. F. Molina, and S. Pernich (2022), Emplacement conditions and exhumation of the Varvarco Tonalite and associated plutons from the Cordillera del Viento, Southern Central Andes, Geological Magazine, 159(5), 645-672, doi:10.1017/s0016756821001163.

Cao, X. W., Z. M. Sun, B. C. Huang, and H. B. Li (2022), Magnetic fabric separation and analysis of rock tectonic deformation, Chinese Journal of Geophysics-Chinese Edition, 65(2), 448-470, doi:10.6038/cjg2022P0336.

He, X., Q. Shen, K. Jiang, C. Z. Li, G. Z. Wu, Y. Z. Ran, C. S. Jin, and W. T. Liang (2022), Room-and low-temperature magnetic fabrics of fine-grained clastic rocks: A case study of the Cretaceous Huicheng basin, Qinling orogen, Chinese Journal of Geophysics-Chinese Edition, 65(2), 737-753, doi:10.6038/cjg2022P0202.

Hoyer, L., and W. W. Hastie (2022), Variable magma flow in sills: Can a magma source be constrained?, Journal of Volcanology and Geothermal Research, 421, doi:10.1016/j.jvolgeores.2021.107427.

Issachar, R., R. Weinberger, T. Levi, J. Barabasch, and J. L. Urai (2022), Magnetic Fabrics and Petrography of Rocksalts Reveal Preferred Orientation of Anhydrites within a Halite Matrix, Minerals, 12(2), doi:10.3390/min12020192.

Jezek, J., and F. Hrouda (2021), Startlingly strong shape anisotropy of AC magnetic susceptibility due to eddy currents, Geophysical Journal International, 229(1), 359-369, doi:10.1093/gji/ggab486.

Li, L. Y., H. Chang, J. M. Pares, B. Bradak, Z. K. Zhang, X. K. Qiang, C. Guan, and C. Y. Quan (2022), Cenozoic Uplift of Tanggula Range and Tuouohe Basin, Northern Tibet: Insights of the Anisotropy of Magnetic Susceptibility, Frontiers in Earth Science, 10, doi:10.3389/feart.2022.815315.

Martin, S. A., J. L. Kavanagh, and A. J. Biggin (2022), Deciphering syn- and post-emplacement processes in shallow mafic dykes using magnetic anisotropy, Journal of Volcanology and Geothermal Research, 422, doi:10.1016/j.jvol-

geores.2021.107456.
Simon-Muzas, A., A. M. Casas-Sainz, R. Soto, J. Gisbert, T. Roman-Berdiel, B. Oliva-Urcia, E. L. Pueyo, and E. Beamud (2022), Axial longitudinal flow in volcanic materials of the Late Carboniferous-Permian Cadi basin (Southern Pyrenees) determined from anisotropy of magnetic susceptibility, Journal of Volcanology and Geothermal Research, 421, doi:10.1016/j.jvolgeores.2021.107443.
Tong, Y. B., Z. Y. Yang, J. L. Pei, H. Wang, Z. H. Wu, and J. F. Li (2022), Upper Crustal Collapse Reconstructed the Topography and Remodeled the Fault System of the Chuandian Fragment in the Southeastern Edge of the Tibetan Plateau, Evidenced by Anisotropy of Magnetic Susceptibility Data Sets, Tectonics, 41(4), doi:10.1029/2021tc007126.
Venkateshwarlu, M., and S. J. Sangode (2022), Borehole magnetic fabric anomalies in KBH 07 Deccan basalt core from Deep Continental Drilling, western Maharashtra, India, Journal of Earth System Science, 131(2), doi:10.1007/s12040-021-01785-x.
Zamanialavijeh, N., Hosseinzadehsabeti, E., Ferre´, E. C., Hacker, D. B., Biedermann, A. R., and R. F. Biek (2021), Kinematics of frictional melts at the base of the world's largest terrestrial landslide: Markagunt gravity slide, southwest Utah, United States Journal of Structural Geology 153 (2021) 104448.

Magnetic Mineralogy and Petrology, Other

Chen, H., C. Tao, A. Revil, Z. Zhu, J. Zhou, T. Wu, and X. Deng (2021), Induced Polarization and Magnetic Responses of Serpentinized Ultramafic Rocks From Mid-Ocean Ridges, Journal of Geophysical Research-Solid Earth, 126(12), doi:10.1029/2021jb022915.
Di, Y. L., L. S. Zeng, J. Chen, L. Gao, and L. F. Zhang (2021), The exsolution lamellae in basic granulite facies scapolite and its formation mechanism: An example from the granulite in the Ama Drime Massif, southern Tibet, Acta Petrologica Sinica, 37(11), 3435-3444, doi:10.18654/1000-0569/2021.11.11.
Fei, H. Z., Z. D. Liu, R. Huang, S. Kamada, N. Hirao, S. Kawaguchi, C. McCammon, and T. Katsura (2021), Pressure Destabilizes Oxygen Vacancies in Bridgmanite, Journal of Geophysical Research-Solid Earth, 126(12), doi:10.1029/2021jb022437.
He, K., S. C. Zhang, X. M. Wang, J. K. Mi, W. J. Zhang, J. H. Guo, and W. L. Zhang (2021), Pyrolysis of 1-methylnaphthalene involving water: Effects of Fe-bearing minerals on the generation, C and H isotope fractionation of methane from H2O-hydrocarbon reaction, Organic Geochemistry, 153, doi:10.1016/j.orggeochem.2020.104151.
Kraal, P., C. M. Van Genuchten, and T. Behrends (2022), Phosphate coprecipitation affects reactivity of iron (oxyhydr)oxides towards dissolved iron and sulfide, Geochimica Et Cosmochimica Acta, 321, 311-328, doi:10.1016/j.gca.2021.12.032.
Mitra, K., E. L. Moreland, A. L. Knight, and J. G. Catalano (2022), Rates and Products of Iron Oxidation by Chlorate at Low Temperatures (0 to 25 degrees C) and Implications for Mars Geochemistry, Acs Earth and Space Chemistry, 6(2), 250-260, doi:10.1021/acsearthspacechem.1c00379.
Nogueira, V. M. E., P. F. Barbosa, S. Mayanna, A. M. Silva, C. L. B. Toledo, L. E. Lagoeiro, and L. M. de Assis (2022), Characterization of the Crystallographic Preferred Orientation Relationships of the Magnetite-Hematite-Goethite Phase Transformation during Martitization, Minerals, 12(3), doi:10.3390/min12030326.
Odlum, M. L., A. K. Ault, M. A. Channer, and G. Calzolari (2022), Seismicity recorded in hematite fault mirrors in the Rio Grande rift, Geosphere, 18(1), 241-260, doi:10.1130/ges02426.1.
Rodger, A., and E. Ramanaidou (2022), Deconstructing the Iron Boomerang-Quantitative Predictions of Hematite, Ochreous, and Vitreous Goethite Mixtures, Minerals, 12(3), doi:10.3390/min12030381.
Tan, W., C. Y. Wang, S. M. Reddy, H. P. He, H. Y. Xian, and C. M. Xing (2022), Magnetite-rutile symplectite in ilmenite records magma hydration in layered intrusions, American Mineralogist, 107(3), 395-404, doi:10.2138/am-2021-7777.
Wang, C., L. E. Christman, S. L. Klemperer, J. M. Glen, D. K. McPhee, and B. Chen (2022), Assessment of a claimed ultra-low frequency electromagnetic (ULFEM) earthquake precursor, Geophysical Journal International, 229(3), 2081-2095, doi:10.1093/gji/ggab530.
Yoshida, K., Y. Tamura, T. Sato, T. Hanyu, Y. Usui, Q. Chang, and S. Ono (2022), Variety of the drift pumice clasts from the 2021 Fukutoku-Oka-no-Ba eruption, Japan, Island Arc, 31(1), doi:10.1111/iar.12441.

Paleomagnetism

Agarwal, A., L. M. Alva-Valdivia, A. Hernandez-Cardona, R. A. Shukla, G. Joshi, and K. K. Agarwal (2022), Tectonics, cooling rates and temperatures during emplacement of the Rajmahal traps, India, Journal of Volcanology and Geothermal Research, 424, doi:10.1016/j.jvolgeores.2022.107496.
Beaver, D. G., D. V. Kent, and I. W. D. Dalziel (2022), Paleomagnetic Constraints From South Georgia on the Tectonic Reconstruction of the Early Cretaceous Rocas Verdes Marginal Basin System of Southernmost South America, Tectonics, 41(2), doi:10.1029/2021tc006990.
Bohnel, H., and A. Rodriguez-Trejo (2022), Comment on Garcia et al. (2021) Semicontinuous paleomagnetic record of the last 1 Ma from radiometrically dated igneous rocks (Trans-Mexican Volcanic Belt and surrounding areas) https://doi.org/10.1016/j. jsames.2021.103195, Journal of South American Earth Sciences, 114, doi:10.1016/j.jsames.2021.103684.
Cengiz, M., S. Karabulut, F. Ozcep, B. S. Cabuk, and F. Heller (2021), Paleomagnetic results from Western Anatolia: evidence of microblock rotations after emplacement of the lower Miocene Yuntdag volcanic rocks, Annals of Geophysics, 64(6), doi:10.4401/ag-8699.
Dannemann, S., E. Appel, W. Rosler, U. Neumann, U. Liebke, and D. Nag (2022), Palaeomagnetic indication for India-Asia collision at 12 degrees N and maximum 810 km Greater India extent in the western suture zone, Geophysical Journal International, 229(2), 1193-1211, doi:10.1093/gji/ggab528.
Fu, Q., et al. (2021), Remagnetization of the Jurassic limestones in the Zaduo area, Eastern Qiangtang Terrane (Tibetan Plateau, China): implications for the India-Eurasia collision, Geophysical Journal International, 228(3), 2073-2091, doi:10.1093/gji/ggab402.
Fu, Q., et al. (2022), The Early Cretaceous Zaduo Granite, Eastern Qiangtang Terrane (China)-An Attempt to Constrain its Paleolatitude and Tectonic Implications, Frontiers in Earth Science, 10, doi:10.3389/feart.2022.829593.
Gerritsen, D., B. Vaes, and D. J. J. van Hinsbergen (2022), Influence of Data Filters on the Position and Precision of Paleomagnetic Poles: What Is the Optimal Sampling Strategy?, Geochemistry Geophysics Geosystems, 23(4), doi:10.1029/2021gc010269.
Harris, M. A., J. K. Russell, R. Barendregt, L. A. Porritt, and A. Wilson (2022), Explosive glaciovolcanism at Cracked

Mountain Volcano, Garibaldi Volcanic Belt, Canada, Journal of Volcanology and Geothermal Research, 423, doi:10.1016/j.jvolgeores.2022.107477.

Jiang, N., et al. (2022), Preliminary paleomagnetic results of the Early-Middle Silurian rocks from North Qiangtang Terrane, and its tectonic implications, Chinese Journal of Geophysics-Chinese Edition, 65(3), 1057-1070, doi:10.6038/cjg2022P0065.

Liang, M. J., T. N. Yang, C. D. Xue, D. Xin, Z. Yan, C. Liao, X. Han, Z. P. Xie, and K. Xiang (2022), Complete deformation history of the transition zone between oblique and orthogonal collision belts of the SE Tibetan Plateau: Crustal shortening and rotation caused by the indentation of India into Eurasia, Journal of Structural Geology, 156, doi:10.1016/j.jsg.2022.104545.

Magli, A., S. Branca, F. Speranza, G. Risica, G. Siravo, and G. Giordano (2022), Paleomagnetic dating of prehistoric lava flows from the urban district of Catania (Etna volcano, Italy), Geological Society of America Bulletin, 134(3-4), 616-628, doi:10.1130/b36026.1.

Marton, E., M. Toljic, and V. Cvetkov (2022), Late and post-collisional tectonic evolution of the Adria-Europe suture in the Vardar Zone, Journal of Geodynamics, 149, doi:10.1016/j.jog.2021.101880.

Meng, J., S. A. Gilder, Y. L. Li, Y. Chen, C. Y. Zhang, Z. Y. Zhou, T. Liu, Y. N. Zhao, Z. H. Wang, and C. S. Wang (2022), Remagnetization Age and Mechanism of Cretaceous Sediments in Relation to Dyke Intrusion, Hainan Island: Tectonic Implications for South China and the Red River Fault, Journal of Geophysical Research-Solid Earth, 127(1), doi:10.1029/2021jb023474.

Mittal, T., M. A. Richards, and I. M. Fendley (2021), The Magmatic Architecture of Continental Flood Basalts I: Observations From the Deccan Traps, Journal of Geophysical Research-Solid Earth, 126(12), doi:10.1029/2021jb021808.

Morake, M. A., J. N. F. O'Kennedy, M. W. Knoper, M. de Kock, J. D. Kramers, G. H. Grantham, G. Belyanin, and M. A. Elburg (2022), The age and palaeomagnetism of Jurassic dykes, western Dronning Maud Land: implications for Gondwana breakup, in Large Igneous Provinces and Their Plumbing System, edited by R. K. Srivastava, R. E. Ernst, K. L. Buchan and M. DeKock, pp. 255-284, doi:10.6084/m9.figshare.c.5612838.

Pandit, M. K., A. Pivarunas, and J. G. Meert (2022), Geochemical and palaeomagnetic characteristics of the Vestfold Hills mafic dykes in the Prydz Bay region: implications of a Paleoproterozoic connection between East Antarctica and Proto-India, in Large Igneous Provinces and Their Plumbing System, edited by R. K. Srivastava, R. E. Ernst, K. L. Buchan and M. DeKock, pp. 149-171, doi:10.1144/sp518-2021-33.

Pastor-Galan, D. (2022), From supercontinent to superplate: Late Paleozoic Pangea's inner deformation suggests it was a short-lived superplate, Earth-Science Reviews, 226, doi:10.1016/j.earscirev.2022.103918.

Rotolo, S. G., S. Scaillet, F. Speranza, J. C. White, R. Williams, and N. J. Jordan (2021), Volcanological evolution of Pantelleria Island (Strait of Sicily) peralkaline volcano: a review, Comptes Rendus Geoscience, 353, doi:10.5802/crgeos.51.

Sierra-Rojas, M. I., R. S. Molina-Garza, J. Pindell, R. A. Rodriguez-Rodriguez, and D. Serrano-Garcia (2022), Paleomagnetism, magnetostratigraphy, provenance, and tectonic setting of the Lower Cretaceous of nuclear southern Mexico, Journal of South American Earth Sciences, 115, doi:10.1016/j.jsames.2022.103719.

Vaes, B., L. C. Gallo, and D. J. J. van Hinsbergen (2022), On Pole Position: Causes of Dispersion of the Paleomagnetic Poles Behind Apparent Polar Wander Paths, Journal of Geophysical Research-Solid Earth, 127(4), doi:10.1029/2022jb023953.

Wang, C. X., Y. B. Tong, Z. Y. Yang, X. D. Yang, and X. X. Sun (2022), Early Cretaceous paleomagnetic characteristics of Yuanma Basin, western Hunan and the indications to the structural deformation of eastern Sichuan fold belt, Chinese Journal of Geophysics-Chinese Edition, 65(1), 280-300, doi:10.6038/cjg2021O0482.

Wu, J. T. J., J. Wu, and K. Okamoto (2022), Intra-oceanic arc accretion along Northeast Asia during Early Cretaceous provides a plate tectonic context for North China craton destruction, Earth-Science Reviews, 226, doi:10.1016/j.earscirev.2022.103952.

Xu, Y. C., X. D. Tan, S. Li, Y. L. Li, B. Ran, Y. L. Han, J. P. Sun, and Z. N. Ma (2022), Paleomagnetism of the Greater Indian passive margin sediments from the Upper Cretaceous succession: Evidence for long-delayed remagnetizations and implication for the India-Asia collision, Journal of Asian Earth Sciences, 229, doi:10.1016/j.jseaes.2022.105165.

Xu, Y., B. F. Han, W. Liao, and A. Li (2022), The Serpukhovian-Bashkirian Amalgamation of Laurussia and the Siberian Continent and Implications for Assembly of Pangea, Tectonics, 41(3), doi:10.1029/2022tc007218.

Yu, L., et al. (2022), New Paleomagnetic and Chronological Constraints on the Late Triassic Position of the Eastern Qiangtang Terrane: Implications for the Closure of the Paleo-Jinshajiang Ocean, Geophysical Research Letters, 49(2), doi:10.1029/2021gl096902.

Stratigraphy

Capraro, L., et al. (2022), The Monte San Nicola section (Sicily) revisited: A potential unit-stratotype of the Gelasian Stage, Quaternary Science Reviews, 278, doi:10.1016/j.quascirev.2021.107367.

Hillaire-Marcel, C., and A. de Vernal (2022), A comment about "A sedimentary record from the Makarov Basin, Arctic Ocean, reveals changing middle to Late Pleistocene glaciation patterns" (Quat. Sci. Rev., 270 (2021), p. 107176) from W. Xiao, L. Polyak, R. Wang, C. Not, L. Dong, Y. Liu, T. Ma, T. Zhang, Quaternary Science Reviews, 279, doi:10.1016/j.quascirev.2021.107239.

Liu, C. C., H. F. Qin, E. C. Ferre, W. Wang, K. He, and C. L. Deng (2022), Importance of Hematite Self-Reversal in Al-Rich Soils Magnetostratigraphy: Revisiting the Damei Red Soil Sequence in the Bose Basin, Southern China, Journal of Geophysical Research-Solid Earth, 127(4), doi:10.1029/2021jb023165.

Lodowski, D. G., A. Pszczolkowski, A. Wilamowski, and J. Grabowski (2022), The Jurassic-Cretaceous transition in the High-Tatric succession (Giewont Unit, Western Tatra Mts, Poland) integrated stratigraphy and microfacies, Acta Geologica Polonica, 72(1), 107-+, doi:10.24425/agp.2021.137712.

Lu, H. J., M. G. Malusa, Z. Y. Zhang, L. C. Guo, X. H. Shi, J. C. Ye, S. P. Sang, S. F. Xiong, J. W. Pan, and H. B. Li (2022), Syntectonic Sediment Recycling Controls Eolian Deposition in Eastern Asia Since similar to 8 Ma, Geophysical Research Letters, 49(3), doi:10.1029/2021gl096789.

Marton, E., R. Pipik, D. Starek, E. Kovacs, M. Vidhya, A. Swierczewska, A. K. Tokarski, R. Vojtko, and S. Schlogl (2022), Enhancing the reliability of the magnetostratigraphic age assignment of azimuthally nonoriented drill cores by the integrated application of palaeomagnetic analysis, field tests, anisotropy of magnetic susceptibility, and the evolution of the endemic fauna as documented on the upper Miocene limnic deposits of the Turiec Basin

(Western Carpathians), Aapg Bulletin, 106(4), 803-827, doi:10.1306/10042120019.
Pervushov, E. M., I. P. Ryabov, V. B. Seltser, I. Walaszczyk, E. A. Kalyakin, A. A. Guzhikova, E. I. Ilyinsky, and D. V. Khudyakov (2021), Upper Cretaceous Deposits in the Volsk Structural Zone of the East European Platform: Turonian-Lower Campanian of the Kommunar Section: Paper 1. Geological Setting, Benthic Foraminifers, and Magnetostratigraphy, Stratigraphy and Geological Correlation, 29(SUPPL 1), S96-S119, doi:10.1134/s0869593822020046.
Sun, J. M., M. Sheykh, B. F. Windley, M. Talebian, M. M. Cao, N. Ahmadi, and J. G. Sha (2022), Magnetostratigraphic Age Control of the Timing of Tectonic Deformation and the Shifting Depositional Environments in the Dezful Embayment, Iran, Tectonics, 41(1), doi:10.1029/2021tc006881.

New IRM resource!

In an attempt to make IRM Quarterly issues more readily searcheable, an Essential Index of some of the most didacting and useful Quarterly articles and contributions has been created and organized by topic.

Please find the Index on the IRM website at: https://cse.umn.edu/irm/essential-irm-quarterly-index

This is an evolving Index, so expect changes (and additions) along the way.

cont'd. from pg. 1...

Schuele, 1964; Stacey, 1960). In this brief overview, we limit the discussion to the magnitude ellipsoids of second order tensors. While not describing every single parameter or plot (we do report many of the parameters proposed in Table 1), we share some general considerations on reporting and visualizing magnetic anisotropy data that apply to different areas of research employing magnetic fabrics, hoping this will be useful in navigating the anisotropy jungle. A similar article on the selection of anisotropy of magnetic susceptibility parameters was already published by Cañon-Tapia (1994), and we refer the readers to that article for completeness.

On a more general note, it is very common for "magnetic anisotropy" and/or "paleomagnetism" to be referred to as "tools", as has also been done here. However, we take this opportunity to iterate that neither are tools in the sense that they can be applied blindly, but are in fact areas of research in their own right, and a-priori thought should be put into data acquisition and processing schemes, parameters to be used, and data visualization and interpretation. While for the most part we are certainly "preaching to the quire", we hope that given the didactic nature of this article series we are able to make a broader group of users aware of the complexities behind applying paleomagnetism and, in this case, magnetic anisotropy.

2 The jungle of anisotropy parameters

2.1 Susceptibility tensors, eigenparameters and mean susceptibility

From here onwards we will adopt terminology specific to magnetic susceptibility for simplicity, but the reader should be aware that the same applies for determining anisotropy from magnetic remanences also. Anisotropy is normally described by either a second-order symmetric tensor or a combination of mean susceptibility (k_{mean}), principal susceptibilities (k_1, k_2, k_3) and their directions, and parameters describing the degree or shape of the anisotropy. Tensors can be reported as full or deviatoric tensors (Fig. 1), either describing directional susceptibilities or susceptibility differences (see the IRMQ31-1 companion article by Bilardello & Biedermann, 2021). The eigenvalues of these tensors are $k_1 \geq k_2 \geq k_3$ and can be normalized in different ways: for deviatoric tensors, $k_1+k_2+k_3= 0$; while for full tensors, $k_1+k_2+k_3= 3$, $k_1+k_2+k_3= 1$, or $k_1+k_2+k_3= 3k_{mean}$ are commonly used (more on k_{mean} or k_m, for brevity, below). These provide equivalent information, and it is normally clear from the reported values what normalization was used. However, note that the ranges adopted by some parameters defining anisotropy degree, magnetic lineation and foliation depend on the definition and normalization of k_m and the eigenvalues. Therefore, a clear description of how data are processed and presented will avoid confusion. Also note that for remanence anisotropy, a further normalization may be made to the applied field when determining anisotropy of anhysteretic susceptibility (McCabe et al., 1985). For a discussion on normalization and the different anisotropy types we refer to the IRMQ30-2 article

Parameter	Range Σ = 1	Reference	Parameter	Range Σ = 1	Reference
Anisotropy degree					
Anisotropy degree, P or P_2= k_1/k_3	1 − ...	Nagata (1961)	Percent anisotropy= $(k_1\text{-}k_3)2k_m$	0 − 1.5	Khan (1962)
Orientation strength, C= $\ln(k_1/k_3)$	0 − ...	Woodcock (1977)	Absolute anisotropy= $(k_1\text{-}k_3)/k_2$	0 − ...	Rees (1966)
Percent anisotropy= $100(k_1\text{-}k_3)/k_1$	0 − 100	Graham (1966)	Corrected anisotropy, P' or P_J= $\exp\{2[(n_1\text{-}n)^2+(n_2\text{-}n)^2+(n_3\text{-}n)^2]\}^{1/2}$	1 − ...	Jelinek (1981)
Percent anisotropy, %A= $100(k_1\text{-}k_3)/k_m$	0 − 300	Taira (1989)	Deviatoric Susceptibility, K'= $\{[(k_1\text{-}k_m)^2+(k_2\text{-}k_m)^2+(k_3\text{-}k_m)^2]/3\}^{1/2}$	0 − …	Jelinek (1984)
Total anisotropy, H= $(k_1\text{-}k_3)/k_m$	0 − 3	Owens (1974)	$\Delta kH = k_1\text{-}k_3$	0 − 1	Owens & Rutter (1978)*
Lineation					
Lineation*, L= k_1/k_2	1 − ...	Balsley & Buddington (1960)	Lineation degree= $2k_1/(k_2+k_3)$	1 − ...	Hrouda et al. (1971)
Normalized lineation, L= $(k_1\text{-}k_2)/k_m$	0 − 3	Khan (1962)	Lineation, %L= $(k_1\text{-}k_2)100/k_m$	0 − 300	Taira (1989)
Lineation, L= $(k_1+k_3)/2k_2$	1 − ...	Urrutia-Fucugauchi (1980)	$\Delta kL = k_1\text{-}k_2$	0 − 1	Owens & Rutter (1978)*
Foliation					
Foliation*, F= k_2/k_3	1 − ...	Stacey et al. (1960)	Foliation degree= $2k_2/(k_1+k_3)$	0 − 2	Urrutia-Fucugauchi (1980)
Foliation, F= 1-(k_3/k_2)	0 − 1	Porath (1971)	Excess Susceptibility= $(k_1+k_2)/2\text{-}k_3$	0 − 0.5	Granar (1958)
Normalized foliation, F= $(k_2\text{-}k_3)/k_m$	0 − 1.5	Khan (1962)	Foliation, %F= $(k_2\text{-}k_3)100/k_m$	0 − 150	this article***
Foliation, F= $(k_1+k_2)/2k_3$	500 − 500	Balsley & Buddington (1960)	$\Delta kF = k_2\text{-}k_3$	0 – 0.5	this article***
Shape					
Prolateness= $(k_1\text{-}k_2)/(k_2\text{-}k_3)$	0 − ...	Khan (1962)	E-factor, F/L= k_2^2/k_1k_3	0 − ...	Hrouda et al. (1971)
Prolateness= $(2k_1\text{-}k_2\text{-}k_3)/(k_2\text{-}k_3)$	1 − ...	Urrutia-Fucugauchi (1980)	Difference shape factor, U= $(2k_2\text{-}k_1\text{-}k_3)/(k_1\text{-}k_3)$	-1 − 1	Jelinek (1981)
Oblateness= $(k_2\text{-}k_3)/(k_1\text{-}k_2)$	0 − ...	Khan (1962)	Shape indicator= $[k_3(k_1\text{-}k_2)]/[k_1(k_2\text{-}k_3)]$	0 − ...	Stacey et al. (1960)
Oblateness= $(k_1+k_2\text{-}2k_3)/(k_1\text{-}k_2)$	1 − ...	Urrutia-Fucugauchi (1980)	Shape parameter or angle, V= $\sin^{-1}[(k_2\text{-}k_3)/(k_1\text{-}k_3)]^{1/2}$	0 − 90	Graham (1966)
Shape gradient, K= $\ln(k_1/k_2)/\ln(k_2/k_3)$	0 − ...	Woodcock (1977)	Shape parameter, T= $(2n_2\text{-}n_1\text{-}n_3)/(n_1\text{-}n_3)$	-1 − 1	Jelinek (1981)
R-factor, L/F= k_1k_3/k_2^2	1 −...	Stacey et al. (1960)**	Ellipsoid shape= $(k_1\text{-}k_2)(2k_1\text{-}k_2\text{-}k_3)/(k_2\text{-}k_3)(k_1+k_2\text{-}2k_3)$	0 − ...	Urrutia-Fucugauchi (1980)
q-factor, L/F= $(k_1\text{-}k_2)/[(k_1+k_2)/2\text{-}k_3]$	0 − 2	Granar (1958)	Shape indicator= $(k_1k_3\text{-}k_2^2)/(k_1k_2\text{-}k_1k_3)$	-1 − 0	Urrutia-Fucugauchi (1980)
Strain indicator= $(k_1k_3\text{-}k_2k_3)/(k_2^2\text{-}k_1k_3)$	-… − 1	Flinn (1962)			

Table 1. Broad selection of anisotropy parameters that have been proposed. Note how many are interrelated: e.g., lineation and foliation parameters are, in truth, categories of shape parameters and in some of their expressions are included in many of those (e.g., q= ΔkL/Excess Susceptibility). *Also, other parameters, e.g., ΔkH, ΔkL (Owens & Rutter, 1978) or %L (Taira, 1989) were already used by others (e.g., Granar, 1958) or Khan (1962)) nested in other parameters or simply normalized (e.g., by k_m and/or expressed as percentage), so that their origin/original use is not obvious. For example, ΔkF, un-normalized, had not been defined before, but its normalized counterpart was already defined by Khan (1962) as for ΔkL**Note that Stacey et al. (1960) calculated L, and F (and therefore R) using the differences of the demagnetizing factors (N_2-N_1 and N_3-N_2, which may be compared to k_1/k_2 and k_2/k_3, respectively).***These parameters are yet unpublished to the best of our knowledge, and we are therefore jokingly "claiming" them here as a testament to the seemingly endless possibility of anisotropy parameters.

by Bilardello (2020). Though k_m is seemingly an easy parameter, several ways of calculating k_m exist. The simplest calculation is that of an arithmetic mean, i.e., k_m= ⅓($k_1+k_2+k_3$) or $k_1+k_2+k_3$. Because the susceptibility axes are often lognormally distributed, a logarithmic k_m notation (n) is also used, where n (or sometimes n_m)= $(n_1+n_2+n_3)/3$, and n_1, n_2, n_3 are the natural logarithms of the principal susceptibilities. Additional ways of calculating mean susceptibility include geometric means, k_{geom}= $(k_1\cdot k_2\cdot k_3)^{⅓}$, particularly useful where the anisotropy correlates with strain, and the average geometric logarithmic mean k_{geom}= antilog $[(\Sigma_i^N \log k)/n]$, where n is the number of samples (we refer to Tarling & Hrouda (1993) for a discussion of these).

The definition of the eigenvalues is straightforward when these are all positive ($k_1 \geq k_2 \geq k_3 > 0$), but different conventions exist when they are all negative or have mixed signs, for example in carbonate rocks (e.g., Hrouda, 2004). If all eigenvalues are negative, k_3 may be defined as either the smallest in absolute values, or as the most negative. Using absolute values will yield anisotropy parameters that are most close to the known parameters for positive eigenvalues, and may therefore make the most sense. However, when a mix of positive and negative eigenvalues is (more rarely) observed, e.g., due to a superposition of diamagnetic and paramagnetic anisotropies (e.g., feldspar with impurities, Biedermann et al., 2016), then defining k_3 as the most negative value is more intuitive. In this case, however, many anisotropy parameters are not truly defined, and the best way

to proceed should be to describe each fabric component separately (e.g., Černý et al., 2020). In any case, stating which convention is used to define the eigenvalues is always recommended.

2.2 Anisotropy degree and shape

Parameters to describe anisotropy shape and degree, include P (or P_2), P' (or P_J), L, F, Δk, k' amongst many others (see Table 1). Cañon-Tapia (1994) notes that lineation and foliation parameters are necessarily inextricably linked to each other, and both incorporated in other shape parameters that will similarly allow the identification of a fabric with either a prominently developed magnetic foliation or lineation. Note that parameters describing AMS degree also depend on the AMS shape; e.g., an extremely prolate anisotropy with k_3= 0.01 (k_1= 2.98, k_2 = 0.01, k_3= 0.01, using k_1+k_2+k_3= 3) and an extremely oblate anisotropy with the same k_3 (k_1= 1.495, k_2= 1.495, k_3= 0.01) would have Δk= k_1-k_3= 2.97 and 1.485, respectively, and P = 298 and 149.5, respectively. Thus, prolate anisotropies always appear larger compared to the oblate counterpart.

Of the many parameters, we will briefly discuss some of the simplest, and therefore straightforward, or popularly used. For most researchers, a combination of lineation (L), foliation (F), degree of anisotropy (P or P_2), corrected degree of anisotropy (P_J or P'), and the shape parameter (U), or its lognormal-distributed equivalent (T), constitute the "bread and butter" of anisotropy parameters. Balsely and Buddington (1960) suggested defining F as $(k_1 + k_2)/2k_3$, which intuitively makes sense for foliated rocks; however, Stacey et al. (1960) point out that a rock with a lineation but no foliation should by definition have a foliation of unity, which is not the case here. In fact, both L and F calculated this way will reach the same maximum value for two perfectly lineated and foliated samples with the same k_3, which is rather confusing (see Table 1), and we only recommend use of this parameter to compare samples with similar foliation-dominated fabrics with dispersed k_1 and k_2 axes, e.g., for sedimentary fabrics.

Parameters that are based on differences rather than ratios have also been proposed, e.g., the normalized lineation of Khan (1962), L= $(k_1$-$k_2)/k_m$. Tarling & Hrouda (1993) recommend that use of this parameter should be abandoned, albeit merely based on the potential confusion with other lineation parameters also defined "L", though many other similarly defined lineation parameters also existed at the time, including the magnetic lineation (L= $(k_1$-$k_2)100/k_m$) of Taira (1989), which should ideally be termed %L, as we have done here (see Table 1). More to the point, Cañon-Tapia (1994) argues that given the small departure from isotropy typically observed in natural rocks, there is no practical difference between using ratios or difference-parameters. In fact, Ellwood et al. (1988) and Tarling (1983) had already noted that the actual calculation of various parameters reduces to a simple arithmetical combination of the principal susceptibilities, provided that these can be uniquely determined, and consequently, they are all interdependent to some extent. However, it will be shown below that for mixtures of paramagnetic and ferromagnetic minerals with different anisotropies, difference-parameters can prove extremely useful.

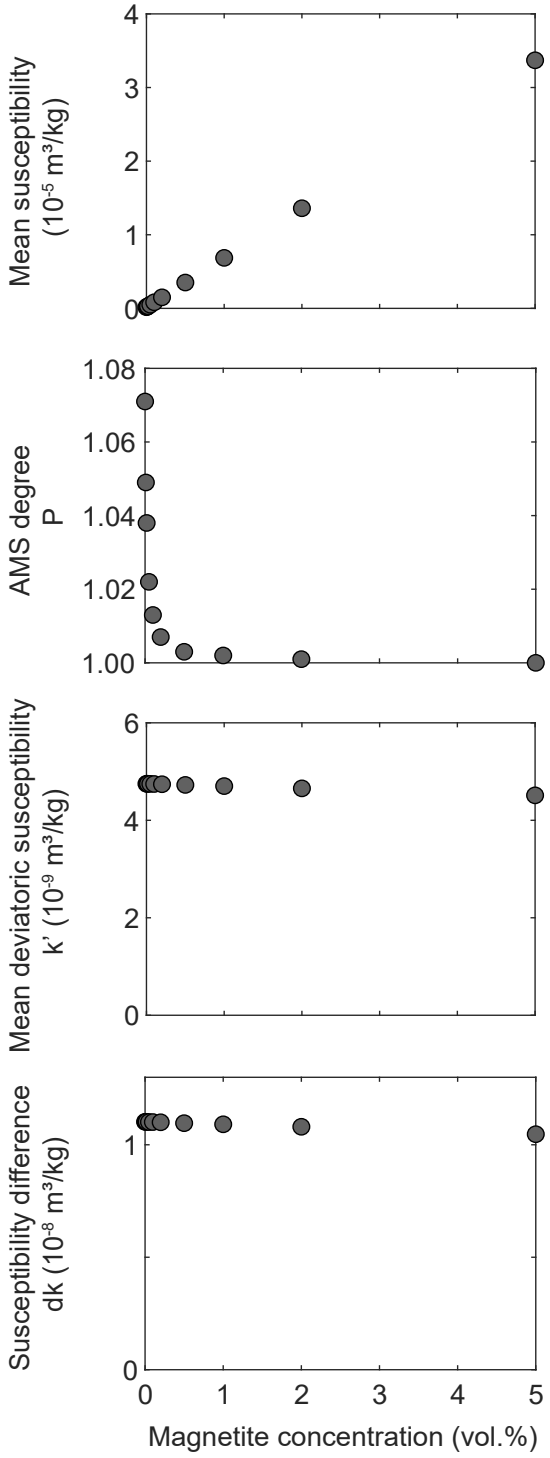

Figure 2. Mean susceptibility and anisotropy parameters for a rock consisting of perfectly aligned biotite and various amounts of isotropic magnetite. The anisotropy degree P decreases quickly with increasing magnetite concentration, and can only be interpreted in conjunction with k_m. The parameters k' and Δk indicate the alignment of biotite independent of magnetite content.

Many commonly used parameters (L, F, P...) have the advantage that they are easily relatable to structural pa-

rameters, but the disadvantage that they are only valid for full tensors and cannot be applied to deviatoric tensors. Deviatoric tensors are often determined in single crystal studies, as they are more precisely defined because differences are measured directly (e.g., Jelinek, 1996), and because some methods only provide deviatoric tensors. Additionally, P and related anisotropy parameters need to be interpreted in conjunction with k_m, when determining contributions to the overall fabric. For example, a rock consisting of 100% perfectly aligned olivine will have a P value of 1.07, which corresponds to the single crystal anisotropy of olivine (when the olivine is not perfectly aligned, the P-value will be lower) (Fig. 2). When isotropic secondary magnetite is added to this rock, the P-value rapidly decreases, and drops below 1.01 as the magnetite content becomes larger than 0.2 vol% (Fig. 2). Therefore, this rock's P-value will appear nearly isotropic, leading to the misinterpretation that the rock is almost undeformed even though the olivine is perfectly aligned. When interpreting P in conjunction with k_m, it becomes clear that even a P-value of 1.01 for a high k_m may indicate strong alignment of the paramagnetic minerals. On the other hand, difference-parameters such as Δk or k' reflect the anisotropy of the olivine independently of the magnetite content, avoiding misinterpretation of complex fabrics (Fig. 2).

2.3 Units of anisotropy parameters

Eigenvalue normalization not only affects parameter ranges (cf. 2.1), but also bears effects on the units of the parameters. Without any normalization, the units of the eigenvalues and their mean will reflect the quantities measured, i.e., the susceptibility or remanence, and these will vary depending on whether they are mass- (e.g., m^3/kg, Am^2/kg) or volume-normalized (e.g., dimensionless, SI, or A/m), or additionally normalized by field to convert remanences into susceptibilities (see Bilardello, 2020, IRMQ30-2, for a discussion on normalization). If un-normalized eigenvalues are used, then the difference parameters will maintain the same units, whereas parameters based on ratios will all be dimensionless. It is of paramount importance, however, that some normalization is performed if the parameters are to be compared among different rocks, possibly even within the same lithology. Normalizing difference-parameters by k_m will generate a dimensionless parameter, which is inherently easier to compare among samples; however, one always needs to bear in mind that k_m and the difference parameters may not be carried by the same minerals, so that normalized parameters are only seemingly easier to compare, as demonstrated in the previous section.

2.4 Terminology for fabric shape

Finally, throughout the years a wide terminology has been used to refer to the different fabric shapes, regardless of how these are calculated. Terms include "flattened ellipsoid", "disk-shaped", "uniaxial girdles", "oblate" fabrics (also, "oblateness"), "constricted ellipsoids", "elongated ellipsoids", "rod-shaped", "uniaxial clusters", "lineated" or "prolate" fabrics ("prolateness") (e.g., Borradaile & Jackson, 2004, 2010; Woodcock, 1977). Borradaile & Jackson (2004) note that terms such as "flattened" and "constricted" used in structural geology are meaningless in the context of magnetic anisotropy, and geometrical descriptors are more appropriate. A flattening or constrictional strain field is expected to align all grains with their long axes in a plane or along a preferred direction, respectively. However, the single crystal principal magnetic susceptibility axes do not necessarily correspond to the mineral shape. For example, for most amphiboles, the maximum susceptibility is along the crystallographic [010] axis, but the longest axis is normally [001]. Similarly, the maximum susceptibility of most clinopyroxenes is at 45° to the [001] crystallographic axis, which is the longest axis (e.g., Biedermann, 2018). Other terms, such as "sedimentary fabrics" for oblate ellipsoids of sediments and sedimentary rocks, with scattered k_1 axes within the sedimentary bedding plane and subvertical k_3 axes, are also widely used and appropriate in the right context. However, we do recommend that defining fabrics by a generic "type", for example "type A for oblate fabrics" and "type B for prolate", is unnecessary and confusing.

3. Data visualization – finding the right plot and "more processed" parameters

3.1. Fabric strength and shape

As for the parameters, certain plots are more appropriate than others for different applications, exactly because they use the same, or comparable, derived quantities. For example, the Flinn diagram (Flinn, 1962) which plots L (k_1/k_2) versus F (k_2/k_3), with origin at F, L = 1, 1, is often used in structural geology to evaluate petrofabrics (Fig. 3a). Shape, on these diagrams, is represented by the slope of a line connecting the origin to the datapoint, and quantified by the confusingly named parameter k= (L-1)/(F-1), which has the further inconvenience of being asymmetric, so that oblate ellipsoids have $1 > k \geq 0$ whereas prolate ellipsoids have $\infty \geq k > 1$. A disadvantage of the Flinn diagram is that weak anisotropies are clustered near the origin, which can make data hard to discern and evaluate their shapes. This effect is overcome on the Ramsay diagram (Ramsay, 1967), also derived for structural applications, where the logarithms of the eigenvalues are used, so that the origin is at 0, 0 and its shape parameter $K = \ln(L)/\ln(F)$.

Unlike Flinn's shape parameter k, Jelink's (1981) U and T parameters range symmetrically between U or T= +1 for oblate ellipsoids and U or T= -1 for prolate ellipsoids, noting, however, that U is zero when k_1-k_2 = k_2-k_3, while T= 0 when $k_1/k_2 = k_2/k_3$.

As other parameters, these shape parameters are also interrelated, so that T, which may also be expressed as ($\ln F$-$\ln L$)/($\ln F$+$\ln L$), relates to Ramsay's K as T= (1-K)/(1+K), whereas U may also be expressed as (F-L)/(F+L). Likewise, Jelinek's (1981) P_J parameter $P_J = \exp\{2[(n_1-n)^2+(n_2-n)^2+(n_3-n)^2]\}^{1/2}$ relates to Nagata's (1961) P parameter (k_1/k_3) as $\ln(P_J) = \ln(P)\cdot\{1+[(T^2)/3]\}^{1/2}$.

The Jelinek diagram (Fig. 3b), which plots P_J versus the shape parameter T, is popular in the rock-magnetic

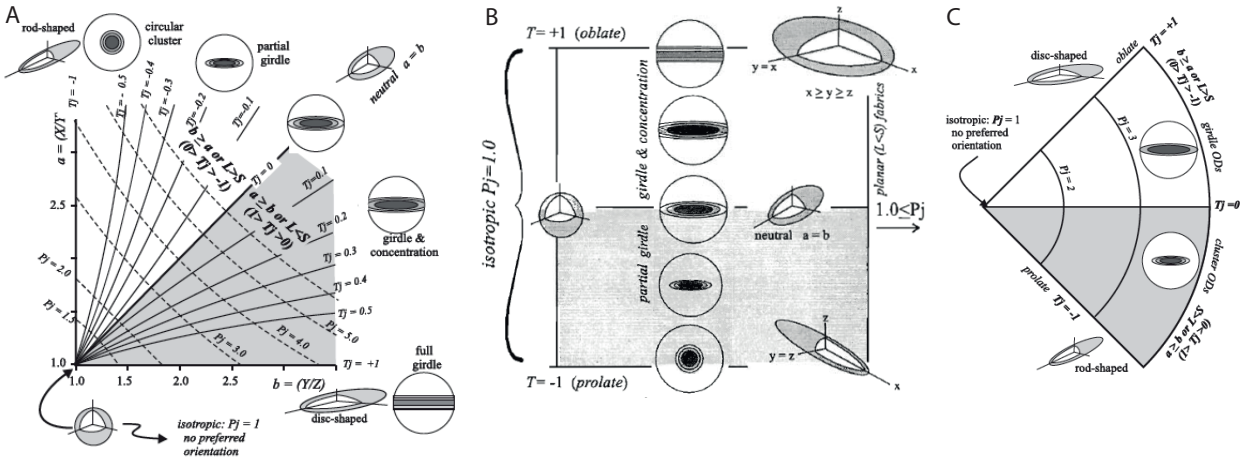

Figure 3. a) Flinn diagram of L versus F, with superimposed curves for $T_{(J)}$ and P_J to demonstrate the relationship between these parameters in this space; b) Jelinek plot of T versus P_J, which avoids the clustering of low anisotropy data towards the origin of the Flinn diagram, yet introduces distortion of the same data (see text for details); c) Polar plot of $T_{(J)}$ (diagram arc-length) and P_J (diagram radius) of Borradaile & Jackson (2004). Original figures by Borradaile & Jackson (2004 and 2010).

community. Compared to the Flinn diagram, this plot has the advantage of expanding the region of low anisotropy; however, expanding this area of the plot necessarily increases the uncertainty around data, so that slight shape differences for weakly anisotropic fabrics appear just as significant as for larger degrees of anisotropy. In general, at low anisotropy degrees, shapes are poorly defined and subject to large uncertainty. Moreover, for perfect isotropy (P_J= 1) the fabrics are spherical by definition, so any values of T at this point are not real, presenting a "non-possible" region, or axis, within the diagram itself.

To obviate for these issues, Borradaile & Jackson (2004) proposed a polar plot in which P_J is the radius and T is the arc-length, which extends from 0 to π/4, representing increasingly oblate distributions, and from 0 to -π/4, representing increasingly prolate ellipsoids (Fig. 3c). Borradaile & Jackson (2010) also extended the polar plot for negative values of P_J, making the plot symmetrical about the origin (not shown here), so that the negative P_J oblate field is on the bottom-left, while the prolate negative P_J field on the top-left part of the plot, allowing representation of diamagnetic fabrics on the same diagram, if the convention of k_1 = largest negative susceptibility is used and substituting the terms in Jelinek's (1981) formula with $\ln(k_1/k_m)$ and so on.

When representing data from the same lithology and/or when there is not much variation among the fabrics of different specimens, another useful plot shows the cumulative distributions of the bootstrapped eigenvalues, introduced by Tauxe et al. (2018) (Fig. 4). Here, the bootstrapped individual eigenvalues are plotted with the intervals containing 95% of their means, versus their cumulative distribution. Strongly overlapping distributions of the three eigenvalues readily indicate more isotropic fabrics, whereas non-overlapping distributions indicate unique eigenvalues and thus triaxial (or neutral) fabrics. Likewise, overlapping k_1 and k_2, but distinct k_3 distributions indicate fabrics that tend to oblate, while overlapping k_2 and k_3, but distinct k_1 distributions indicate prolate fabrics. The larger the "spread" between k_1 and k_3, the stronger the anisotropy. Because the distributions are bootstrapped, including specimen-data or site-mean data that carry substantially different anisotropies will affect the cumulative distribution, so that the function becomes

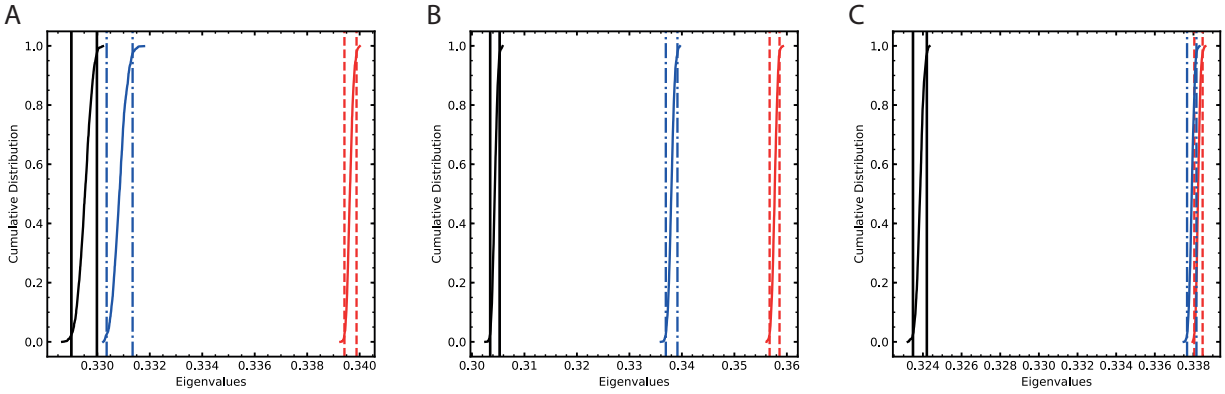

Figure 4. Cumulative distribution of the eigenvalues: a) triaxial-prolate data, note the similar magnitude of the minimum and intermediate eigenvalues that do not however fall within each other's 95% confidence intervals, black solid lines for the minimum and blue dash-dot lines for the intermediate, yet they are both much smaller than the maximum eigenvalue distribution, red line, indicating a dominantly prolate fabric; b) triaxial data showing significant spacing and no overlap between the three eigenvalue distributions; c) perfectly oblate data, with indistinguishable maximum and intermediate eigenvalue distributions, much larger than the minimum. Data from Bilardello (2021), plotted using the PmagPy software package of Tauxe et al. (2016).

somewhat blocky. Such observation will alert the user that one or more fabric determinations may either be different from the others, or problematic. In this respect, however, to some extent both the sampling scheme and data do dictate which plots one should use, so that if there is a range in anisotropy degree and/or shape, the more isotropic data will be strongly clustered on a Flinn diagram, whereas the cumulative distribution plot will be somewhat off.

Triangular or ternary diagrams of the normalized eigenvectors have also been used for eigenvalues, with apices at k_1=1, k_2= 0.5, and k_3=0.33 (Mark, 1974; Mark & Andrews, 1975), and are analogous to Harland and Bayly's (1958) stress plot (Fig. 5). Such plots have a curved line separating the fields for clustered (lineated) and girdled (foliated) fields, and the overall lack of symmetry makes them somewhat difficult to interpret (Fig. 5a). Nevertheless, ternary diagrams are commonly used within the glaciology community, for example, where fabric elongation (1- k_2/k_1) is plotted against fabric isotropy (k_3/k_1). In this diagram, the apices represent three end-member fabric shapes: [1 - (k_2/k_1)= 0; k_3/k_1 = 1] for isotropic fabrics; [1 - (k_2/k_1)= 0; k_3/k_1= 0] for planar girdles; and [1 - (k_2/k_1)= 1; k_3/k_1 = 0] for perfect axial clusters. (Benn, 1994).

As a final remark about different ways of plotting anisotropy parameters, one must bear in mind that for perfect fabrics, ranging from neutral to infinitely prolate and oblate, the magnitudes of the eigenvalues vary asymmetrically from being equal to one axis being unique and infinitely long (k_1) and the other two equal and infinitely small (k_2= k_3) for the prolate case, or one being infinitely small (k_3), and the other two equal and infinitely long (k_1= k_2) in the oblate case. Therefore, for prolate fabrics with finite, not infinite, principal axes, the maximum eigenvalue will always be twice the size of the maximum (and intermediate) eigenvalues of the oblate counterpart (see Fig. 5a). This condition necessarily generates an inherent asymmetry in any possible plot and shape parameter, as mentioned above for Flinn's k, Ramsey's K, or Jelinek's P_J, for which prolate fabrics will always have more range. Moreover, incrementally reducing prolateness to neutrality and subsequently increasing oblateness, the path will not follow a linear trajectory (cf. Fig. 1.6 of Tarling and Hrouda, 1993). For all the considerations made so far, every plot has its faults, so that choice of diagram is mostly a matter of preference, and to some extent dictated by the data at hand and/or sampling strategy.

3.2. Fabric orientation.

Plotting eigenvector orientation data on an equal area lower hemisphere stereonet is the most widely used and appropriate fabric orientation representation (Fig. 6a). However, how to represent the confidence of a mean eigenvector of a group of samples varies among users. Granted that confidence circles (e.g., α_{95} circles) should never be used for anisotropy, Jelinek's (1978) confidence ellipses are probably the most commonly used method of representing uncertainties (Fig. 6b). Alternatively, Constable and Tauxe (1990) developed a bootstrap representation for anisotropy data, where the bootstrap "cloud" distribution of eigenvectors is plotted on a stereonet (Fig. 6c). The bootstrap method relies on the assumption that the full statistical variability is represented in the data set, and therefore about 20 or more specimens should be included. However, if the standard deviations around the tensor elements are normally distributed it is possible to perform a parametric bootstrap on fewer specimens, possibly as few as six (Tauxe et al., 1998). The mean eigenvectors of the distribution and a contour line enclosing 95% of the bootstrapped eigenvectors may also be represented instead, the bootstrap ellipses, yielding uncertainties around the means that, for sufficient specimen numbers, are virtually identical to the Jelinek (1978) ellipses (Fig. 6d). The "real-data" example in Fig. 6 highlights that when sufficient numbers of specimens are present, n= 41 in this case, not only the Jelinek and bootstrap confidence ellipses, and bootstrap distributions are comparable, but demystifies the notion that the bootstrap method tends to minimize the distributions, granted that the original data should always be shown or, at a minimum, reported.

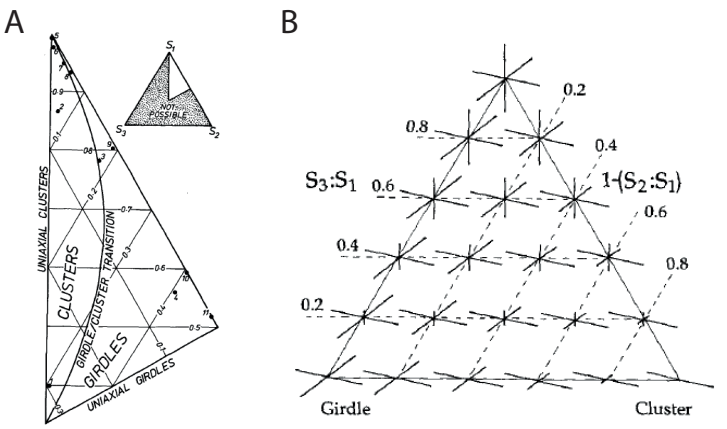

Figure 5. Triangular diagrams: a) undistorted ternary diagram, after Woodcock (1977), with the isotropic condition at the bottom, oblate fabrics, or girdles, at the right, and prolate fabrics, or clusters, at the top. The inset demonstrates how the maximum eigenvalues must be between 0.3 (1) and 1 (3), while the intermediate eigenvalue cannot exceed 0.5 (1.5) and the minimum 0.3 (1), when normalized so that their sum equals 1 (3); b) "distorted" ternary diagram of Benn (1994) with the isotropic condition at the top, elongated fabrics at the lower right, and flattened fabrics at the lower left. Note that although we argued above that terms such as "constricted" or "elongated" should be avoided when describing magnetic fabrics, we maintained "Fabric Elongation" to remain consistent with the descriptions of Benn (1994), whereas "Fabric Flattening" was chosen by us for consistency.

An alternative way of representing directional data is to plot colormap images of the anisotropy, which is more commonly used by anisotropy modelers and/or for seismic anisotropy. On such plots, the color reflects the magnitude of directional susceptibility, which includes the values of principal susceptibility directions, but provides more complete information on the variation of susceptibility in 3D. However, note that some color scales may work better than others and not only for questions of accessibility (e.g., color-blindness). For example, different color scales are shown in Fig. 7 for the susceptibilities of

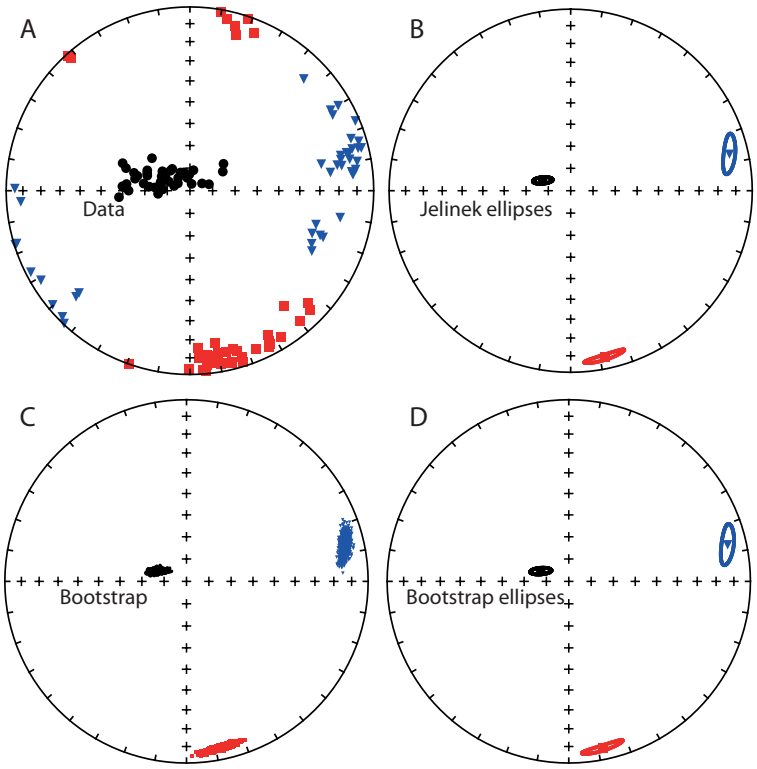

Figure 6. Eigenvector orientation data plotted on lower hemisphere stereonets (red squares, blue triangles and black dots are the maximum, intermediate and minimum eigenvectors, respectively): a) original data; b) Jelinek confidence ellipses; c) bootstrap cloud distribution; d) bootstrap confidence ellipses. Data from Bilardello (2021), plotted using the PmagPy software package of Tauxe et al. (2016).

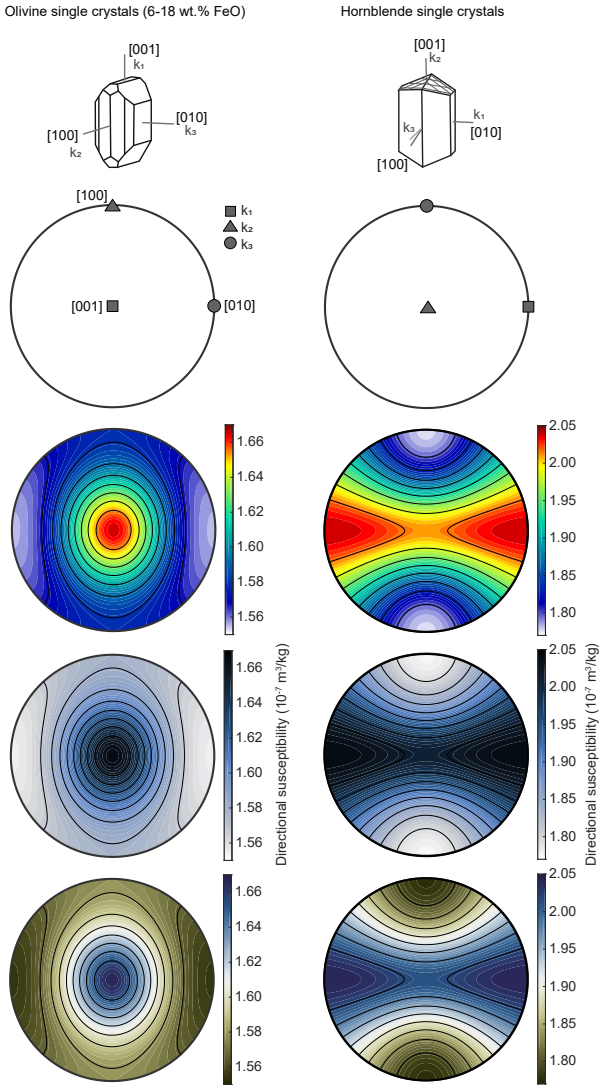

Figure 7. Paramagnetic anisotropy of olivine (left) and hornblende (right) single crystals. The sketches show the principal susceptibility axes with respect to the crystallographic axes. Lower hemisphere equal area stereoplots show either the orientation of the principal susceptibility axes or color-coded directional susceptibility in 3D. Note that colormaps show a single tensor, while multiple tensors can be represented by the standard stereoplot. Different colormaps of the same data include 'standard' rainbow, which is often used but distorts data visually, enhancing the red colors, and perceptually uniform sequential ('oslo') and diverging ('broc') colormaps from Crameri (2018). Contours further highlight the visual distortion of the rainbow colormap.

olivine and hornblende single crystals, in relation to their crystallographic axes. The figure demonstrates that the rainbow scale visually distorts data because the yellow is the brightest color, attracting the eye the most, yet it is not located at the center of the map, whereas the green shades form a wide band with low perceived color contrast, opposed to the narrow band with high contrast of the red tones, so that the maximum eigenvector location appears more clustered than the minimum counterpart (Crameri, 2018; Crameri et al., 2020): a bimodal scale with a neutral (white) color midway between the maximum and minimum eigenvector locations is more appropriate. In any case, adding contour lines to counter any distortion effect is recommended; similar considerations and plotting improvements have been made by Ramon Egli in the context of FORC diagrams, from which we have extensively "borrowed" here and whom we thank for the discussion.

To some degree the choice of plot will be defined by the data used, e.g., colormaps are great for single specimens, while bootstrapped data can only be applied when averaging a sufficient number of samples. Other than that, it is mainly the authors' (or sometimes the reviewers') personal preference that will define the type of plots used.

4. Finding the way through the jungle

To summarize, we put together a number of recommendations for processing and visualizing anisotropy data. One important topic that was left out, however, is that of data significance and uncertainties, which will be covered in a subsequent article.

The first step is to determine whether the data are from full or deviatoric tensors, which will likely correspond to the type of work one performed. These require different parameters, whereby only k', Δk and U work for deviatoric tensors, and P, P_J, T, L, F, etc., are only applicable to full tensors.

Data should be normalized, so that they are comparable among specimens: choice of normalization will also dictate the ranges of calculated parameters, so care is needed if comparisons to other data are to be made. For difference-parameters, a normalization by k_m is useful,

bearing in mind the caveats when several carrier minerals contribute to the magnetic anisotropy. Also note that the definition and normalization of k_m controls the ranges adopted by other parameters.

Of the multitude of parameters proposed in the literature many different measures for F exist, for example, and each bears some implications. What is the purpose of the study and target audience? For structural applications one should use parameters that are more easily correlated with similar data (e.g., P, L, F). For separating fabric components, k' and Δk can be interpreted without knowing k_m, avoiding the caveat referred to above. If data are to be compared to single-crystal data, then k' and Δk etc., are also the most appropriate, since most single crystal data are reported with these parameters. For paleomagnetic applications, for example anisotropy corrections for deflection of remanences or paleointensity, one must use full remanent tensors that characterize the mineral sub-populations carrying the remanence. These include the appropriate type of anisotropy (of TRM, ARM or IRM) to correct a natural or laboratory remanence, in the correct units, and to isolate the magnetic carriers in the grain size range of interest.

One should next evaluate the amount of data, which dictates choice of plot and parameters: for many specimens, plots that involve bootstrap confidence bounds may be used, but for fewer data, plots that use analytical uncertainties are more appropriate.

Next, the range and distribution of the data will inform what plot is better-suited. Whether all data are comparable among each other, or whether they necessarily need to be grouped by sites or different lithologies, and whether site-means may be plotted together, will dictate which plots one can use. These considerations also fall within the scope of the study and will dictate what "shape and magnitude" plots one should use, particularly with linear versus logarithmic distributions, and whether cumulative distribution plots are appropriate.

Finally, all parameters and visualization options have their advantages and limitations (e.g., large uncertainty in anisotropy shape for low anisotropy degrees is amplified by the Jelinek plot). It is important to be aware that the choices made bear implications for each parameter and plot.

References

Balsley, J. R., & Buddington, A. F. (1960). Magnetic susceptibility anisotropy and fabric of some Adirondack granites and orthogneisses. American Journal of Science, 258A, 6–20.

Benn, D. I. (1994). Fluted moraine formation and till genesis below a temperate valley glacier: Slettmarkbreen, Jotunheimen, southern Norway. Sedimentology, 41(2), 279–292. https://doi.org/10.1111/j.1365-3091.1994.tb01406.x

Biedermann, A. R. (2018). Magnetic Anisotropy in Single Crystals: A Review. Geosciences, 8(8), 302. https://doi.org/10.3390/geosciences8080302

Biedermann, A. R., & Bilardello, D. (2021). Practical Magnetism VII: Avoiding common Misconceptions in Magnetic Fabric Interpretation. IRM Quarterly, 31(3), 1–18.

Biedermann, A. R., Pettke, T., Angel, R. J., & Hirt, A. M. (2016). Anisotropy of magnetic susceptibility in alkali feldspar and plagioclase. Geophysical Journal International, 205, 479–489.

Biedermann, A. R., Jackson, M., Chadima, M., Hirt, A. M., & Feinberg, J. M. (2020). Beyond the second-order magnetic anisotropy tensor: higher-order components due to oriented magnetite exsolutions in pyroxenes, and implications for palaeomagnetic and structural interpretations. Geophysical Journal International, 223(2), 915–933. https://doi.org/10.1093/gji/ggaa355

Bilardello, D. (2020). Practical Magnetism III: what's what in remanence anisotropy, 30(2), 1–17.

Bilardello, D. (2021). Late Paleozoic Depositional Environments and Sediment Transport Directions of the Itararé Group Rocks From the State of São Paulo, Brazil, Determined From Rock Magnetism and Magnetic Anisotropy. Earth and Space Science, 8(7), 1–20. https://doi.org/10.1029/2021EA001703

Blott, S. J., & Pye, K. (2007). Particle shape: a review and new methods of characterization and classification. Sedimentology, 55(1), 070921092734002-??? https://doi.org/10.1111/j.1365-3091.2007.00892.x

Borradaile, G. J., & Jackson, M. (2004). Anisotropy of magnetic susceptibility (AMS): magnetic petrofabrics of deformed rocks. In Martin-Hernandez, F., Luneburg, C. M., Aubourg, C. and Jacskon, M. (eds). Magnetic Fabric: Methods and Applications. Geological Society, London, Special Publications (pp. 299–360).

Borradaile, G. J., & Jackson, M. J. (2010). Structural geology, petrofabrics and magnetic fabrics (AMS, AARM, AIRM). Journal of Structural Geology, 32(10), 1519–1551. https://doi.org/10.1016/j.jsg.2009.09.006

Cañón-Tapia, E. (1994). Anisotropy of magnetic susceptibility parameters: Guiedelines for their rational selection. Pure and Applied Geophysics, 142(2), 365–382.

Černý, J., Melichar, R., Všianský, D., & Drahokoupil, J. (2020). Magnetic Anisotropy of Rocks: A New Classification of Inverse Magnetic Fabrics to Help Geological Interpretations. Journal of Geophysical Research: Solid Earth, 125(11), 1–13. https://doi.org/10.1029/2020JB020426

Constable, C., & Tauxe, L. (1990). The bootstrap for magnetic susceptibility tensors. Journal of Geophysical Research, 95, 8383–8395.

Crameri, F. (2018). Geodynamic diagnostics, scientific visualisation and StagLab 3.0. Geoscientific Model Development, 11(6), 2541–2562. https://doi.org/10.5194/gmd-11-2541-2018

Crameri, F., Shephard, G. E., & Heron, P. J. (2020). The misuse of colour in science communication. Nature Communications, 11(1), 5444. https://doi.org/10.1038/s41467-020-19160-7

Ellwood, B. B., Hrouda, F., & Wagner, J. J. (1988). Symposia on Magnetic Fabrics: Introductory Comments. Physics of the Earth and Planetary Interiors, 51, 249–252.

Flanders, P. J., & Schuele, W. J. (1964). Anisotropy in the basal plane of hematite single crystals. Philosophical Magazine, 9(99), 485–490. https://doi.org/10.1080/14786436408222959

Flinn, D. (1962). On folding during three-dimensional progressive deformation. Quarterly Journal of the Geological Society of London, 118, 385–433.

Graham J. W. (1966). Significance of magnetic anisotropy in Appalachian sedimentary rocks. Geophysical Monograph Series, 10, 627–648.

Granar, L. (1958). Magnetic measurements on Swedish varved sediments. Arkiv. f. Geogysik, 3, 1–40.

Harland, W. B., & Bayly, M. B. (1958). Tectonic regimes.

Geol. Mag., 95, 89–104.
Hrouda, F. (2004). Problems in interpreting AMS parameters in diamagnetic rocks. Geological Society, London, Special Publications, 238(1), 49–59. https://doi.org/10.1144/GSL.SP.2004.238.01.05
Hrouda, F., Janak, F., Rejl, L., & Weiss, J. (1971). The Use of Magnetic Susceptibility Anisotropy for Estimating the Ferromagnetic Mineral Fabrics of Metamorphic Rocks, Geol. Rdsch. Geol. Rdsch., 60, 1124–1142.
Jelinek, V. (1981). Characterization of the magnetic fabric of rocks. Tectonophysics, 79, 63–67.
Jelinek, V. (1984). On a mixed quadratic invariant of the magnetic susceptibility tensor. Journal of Geophysics - Zeitschrift Fur Geophysik, 56(1), 58–60.
Jelinek, V. (1996). Measuring anisotropy of magnetic susceptibility on a slowly spinning specimen - basic theory. AGICO Print, 10.
Jelínek, V. (1978). Statistical processing of anisotropy of magnetic susceptibility measures on groups of specimens. Studia Geophisica et Geodetica, 22, 50–62.
Khan, M. A. (1962). The anisotropy of magnetic susceptibility of some igneous and metamorphic rocks. Journal of Geophysical Research, 67(7), 2873–2885. https://doi.org/10.1029/jz067i007p02873
Mark, D. M. (1974). On the interpretation of till fabrics. Geology, 2, 101–104.
Mark, D. M., & Andrews, J. T. (1975). A reexamination of the till fabrics and the origins of some “cross-valley” moraines on Baffin Island. Geol. Foreh. Stockhem Forh., 97, 321–325.
McCabe, C., Jackson, M. J., & Ellwood, B. B. (1985). Magnetic anisotropy in the Trenton limestone: results of a new technique, Anisotropy of Anhysteretic Susceptibility. Geophysical Research Letters, 12(6), 333–336.
Nagata, T. (1961). Rock Magnetism. Tokyo: Maruzen.
Owens, W. H. (1974). Mathematical model studies on factors affecting the magnetic anisotropy of deformed rocks. Tectonophysics, 24, 115–131.
Owens, W. H., & Rutter, E. H. (1978). The development of magnetic susceptibility anisotropy through crystallographic preferred orientation in a calcite rock. Physics of the Earth and Planetary Interiors, 16(3), 215–222. https://doi.org/10.1016/0031-9201(78)90014-6
Porath, H. (1971). Anisotropie der magnetischen Suszeptibilitiit und Siittigungmagnetisierung als Hilfmittel der Gefiigekunde. Geol. Rundsch., 60, 1088–1102.
Ramsay, J. G. (1967). Folding and Fracturing of Rocks. New York: McGraw-Hill.
Rees, A. I. (1966). The Effects of Depositional Slopes on the Anisotropy of Magnetic Susceptibility of Laboratory Deposited Sands. J. Geol., 74, 856–867.
Stacey, F. D. (1960). Magnetic anisotropy of igneous rocks. Journal of Geophysical Research, 65(8), 2429–2442. https://doi.org/10.1029/JZ065i008p02429
Stacey, F. D., Joplin, G., & Lindsay, J. (1960). Magnetic anisotropy and fabric of some foliated rocks from S.E. Australia. Geofisica Pura e Applicata, 47, 30–40.
Taira, A. (1989). Magnetic fabrics and depositional processes. In A. Taira & F. Masuda (Eds.), Sedimentary Facies in the Active Plate Margin (pp. 43–77). Tokyo: Terra Scientific Publishing Company (TERRAPUB). Retrieved from http://www.terrapub.co.jp/e-library/taira/pdf/043.pdf
Tarling, D. H. (1983). Palaeomagnetism. Principles and Applications in Geology, Geophysics and Archaeology. London: Chapman and Hall.
Tarling, D. H., & Hrouda, F. (1993). The Magnetic Anisotropy of Rocks (p. 217 pp.). London: Chapman and Hall.
Tauxe, L., Shaar, R., Jonestrask, L., Swanson-Hysell, N. L., Minnett, R., Koppers, A. A. P., et al. (2016). PmagPy: Software package for paleomagnetic data analysis and a bridge to the Magnetics Information Consortium (MagIC) Database. Geochemistry, Geophysics, Geosystems, 17(6), 2450–2463. https://doi.org/10.1002/2016GC006307
Tauxe, Lisa, Gee, J., & Staudigel, H. (1998). Flow directions in dikes from anisotropy of magnetic susceptibility data: The bootstrap way. Journal of Geophysical Research, 103(B8), 17,775–17,790.
Tauxe, Lisa, Banerjee, S. K., Butler, R. F., & van der Voo, R. (2018). Essentials of Paleomagnetism, 5th Web Edition.
Urrutia-Fucugauchi, J. (1980). Palaeomagnetic studies of Mexican rocks. University of Newcastle upon Thyne.
Woodcock, N. H. (1977). Specification of Fabric Shapes Using an Eigenvalue Model. Geological Society of America Bulletin, 88, 1231–1236.

The IRM
Quarterly

The *Institute for Rock Magnetism* is dedicated to providing state-of-the-art facilities and technical expertise free of charge to any interested researcher who applies and is accepted as a Visiting Fellow. Short proposals are accepted semi-annually in spring and fall for work to be done in a 10-day period during the following half year. Shorter, less formal visits are arranged on an individual basis through the Facilities Manager.

The *IRM* staff consists of **Subir Banerjee**, Professor/Founding Director; **Bruce Moskowitz**, Professor/Director; **Joshua Feinberg**, Assistant Professor/Associate Director; **Maxwell Brown, Peat Sølheid** and **Dario Bilardello**, Staff Scientists.

Funding for the *IRM* is provided by the **National Science Foundation**, the **W. M. Keck Foundation**, and the **University of Minnesota**.

The *IRM Quarterly* is published four times a year by the staff of the *IRM*. If you or someone you know would like to be on our mailing list, if you have something you would like to contribute (*e.g.*, titles plus abstracts of papers in press), or if you have any suggestions to improve the newsletter, please notify the editor:

Dario Bilardello
Institute for Rock Magnetism
University of Minnesota
150 John T Tate Hall
116 Church Street SE
Minneapolis, MN 55455-0128
phone: (612) 624-5049
e-mail: dario@umn.edu
www.irm.umn.edu

UNIVERSITY OF MINNESOTA